A type I interferon response defines a conserved microglial state required for effective neuronal phagocytosis

Authors: Leah C. Dorman[1,2,11#], Phi T. Nguyen[1,3,12#], Caroline C. Escoubas[1], Ilia D. Vainchtein[1], Yinghong Xiao[4], Peter V. Lidsky[4], Haruna Nakajo[1], Nicholas J. Silva[1], Christian Lagares-Linares[1], Ellen Y. Wang[1,5], Sunrae E. Taloma[1,2], Beatriz Cuevas[1,2], Hiromi Nakao-Inoue[1], Brianna M. Rivera[6], Bjoern Schwer[7,10], Carlo Condello[6], Raul Andino[4], Tomasz J. Nowakowski[1,7,8,9,10], Anna V. Molofsky[1,7,9]*

Affiliations:
[1]Departments of Psychiatry and Behavioral Sciences/ Weill Institute for Neurosciences, [2]Neuroscience Graduate Program, [3]Biomedical Sciences Graduate Program, [4]Department of Microbiology and Immunology, [5]UCSF SRTP program, [6]Institute for Neurodegenerative Diseases/Weill Institute for Neurosciences, [7]Kavli Institute for Fundamental Neuroscience, [8]Department of Anatomy, [9]Eli and Edythe Broad Center for Regeneration Medicine and Stem Cell Research, [10] Department of Neurosurgery.

[1-9]University of California, San Francisco, San Francisco, CA.
[10]Chan-Zuckerberg Biohub, San Francisco, CA.

[#]These authors contributed equally.

[11]Twitter: @sculptorofdance
[12]Twitter: @Phi_hD

*Correspondence to:

Anna V Molofsky MD PhD, University of California San Francisco, 1550 4th Street, San Francisco, CA 94158, USA. Tel: 1 (415) 502-3609. anna.molofsky@ucsf.edu, @AnnaMolofskyLab

Summary

Microglia, the innate immune cells of the brain, are exquisitely sensitive to dynamic changes in the neural environment. Using single cell RNA sequencing of the postnatal somatosensory cortex during topographic remapping, we identified a type I interferon (IFN-I) responsive microglia population that expanded with this developmental stressor. Using the marker gene IFITM3 we found that IFN-I responsive microglia were engulfing whole neurons. Loss of IFN-I signaling (*Ifnar1*$^{-/-}$) resulted in dysmorphic 'bubble' microglia with enlarged phagolysosomal compartments. We also observed a reduction in dead cells and an accumulation of neurons with double strand DNA breaks, a marker of cell stress. Conversely, IFN-I gain of function in zebrafish was sufficient to drive microglial engulfment of whole neurons. We identified IFITM3+ microglia

in two murine disease models: SARS-CoV-2 infection and the 5xFAD model of Alzheimer's disease. These data reveal a novel role for IFN-I signaling in regulating efficient neuronal clearance by microglia.

Introduction

Neural circuits undergo dynamic and experience dependent changes in circuit connectivity during brain development, and even subtle alterations in this process are associated with neurodevelopmental diseases[1–4]. Glial cells, including astrocytes and microglia, are essential to physiological neural circuit development and function[5,6]. Microglia in particular are of emerging interest due to their multiple roles in circuit development, including promoting synapse elimination, driving synapse formation, and engulfing whole cells[7,8]. Yet despite this clear evidence of functional heterogeneity, defining the links between gene expression and function remains an active area of investigation[9,10]. One potential reason why these connections are still not completely defined is that glial heterogeneity can be transient, context-dependent, and difficult to capture. For example, while microglia broadly belong to a PU.1-dependent myeloid lineage, much of what distinguishes subsets of microglia from each other depends on dynamic responses to local factors, including cytokines, neuronal activity, and damage-associated molecular patterns[5,11–14]. Thus, defining how CNS contextual cues alter glial states is critical to linking genes to function, particularly for physiological responses that are continuously fine-tuned to maintain homeostasis[15].

In this study, we challenged the developing murine somatosensory system with altered sensory input via whisker-follicle cauterization[16–18] in order to elicit glial responses to an acute but non-inflammatory re-ordering of the neural environment. Single-cell sequencing of somatosensory cortical microglia during the subsequent topographic remapping (https://www.annamolofskylab.org/microglia-sequencing) led to the identification of a population of type I interferon (IFN-I) responsive microglia population that was actively engulfing whole neurons *in situ*. Our data suggest that IFN-I is required for effective microglial phagocytosis, and that in the developing brain, an IFN-I responsive state is associated with clearance of damaged but not yet terminally injured neurons. The IFN-I signature we identified is also detected across pathologies ranging from viral infections to Alzheimer's Disease, raising the possibility that they represent a distinct phagocytic state in those settings. More broadly, our data reveal the potential of single cell transcriptomics following a defined physiological perturbation to identify novel functional subsets of microglia.

Results

Microglia and astrocytes alter their transcriptomes in response to cortical remapping

To elicit glial phenotypes in response to physiologic changes in local circuits, we adapted a well-established barrel cortex remodeling paradigm. Facial whisker lesion before postnatal day 4 (P4) leads to irreversible structural alterations of the cortical topographic map, whereby thalamocortical synapse and cell-rich regions (barrels) separated by septa rearrange around the new sensory input space[16,18–23]. Importantly, because the whisker somatosensory circuit synapses in the brainstem and the thalamus en route to the cortex, whisker lesioning leads to circuit remodeling without inducing injury responses in the cortex (**Fig. 1a**). This paradigm captures astrocytes and microglia during a period of active proliferation and maturation. Cortical astrocytes are present by P0, but proliferate and elaborate their processes between P0-P30[24], while microglia populate the barrel cortex septa between P3 and P5 with full invasion of the barrel centers by P7[25]. Microglia engulf barrel cortex synapses in response to complete whisker ablation[26], suggesting that this paradigm may be useful for studying microglial phagocytic responses.

To elicit rearrangement but not elimination of the whisker map, we unilaterally cauterized 40% of the facial whiskers by removing follicles in alternating rows (B and D) at P2. We examined responses at P5 and P7, following layer 4 barrel coalescence at ~P3-P5 (**Fig. 1a**; [27,28]). For this and all subsequent experiments, we compared contralateral deprived barrel cortex with ipsilateral spared cortex as an internal control. As expected, neonatal whisker removal led to redistribution of the VGLUT2+ thalamocortical axonal boutons in cortical layer 4, whereby the deprived cortical rows (B and D) were smaller with indistinct barrel separation (**Fig. 1b,** [17]). This was reflected as a decreased ratio of VGLUT2 intensity between barrels and septa in layer 4 (**Fig. 1c**). However, mean VGLUT2 intensity across the entire barrel cortex was not significantly different, suggesting that despite redistribution, overall thalamocortical synapse density was preserved (**Fig. 1d, Fig. S1a**). Therefore this model may elicit different microglial states compared to full unilateral whisker loss, which leads to progressive dimming of VGLUT2 intensity[29]. Microglial and astrocyte density were unchanged (**Fig. S1b-e**), and we did not detect any evidence of morphologic or molecular changes often associated with injury responses as measured by GFAP and Iba1 intensity respectively (**Fig. S1f-i**). We conclude that this model leads to a reorganization of the structure of the barrel cortex without provoking gross changes in synapse numbers.

To survey the response of all glia to this topographic remodeling at higher resolution, we performed single cell RNA sequencing of non-neuronal cells in microdissected somatosensory cortex. We used cold protease digestion at 4°C[30] to dissociate the tissue, which preserved most non-neuronal subsets. We found that relative to papain digestion at 34°C, this strategy increased the relative expression of microglial *P2ry12,* which has been associated with a homeostatic microglial state, and substantially decreased expression of *Tnf,* which can be induced in inflammatory or reactive conditions (**Fig. S2a-c**). Fluorescence-activated cell sorting (FACS) was used to recover live cells and enrich microglia ($CD11b^{+}/CD45^{lo}$) to 30% of total cells before single cell sequencing on the 10x Chromium V2 platform (**Fig. 1e, S2d-g**). After quality control (**Fig. S2h-j**), unbiased clustering revealed clusters specific to astrocytes, microglia, oligodendrocyte lineage cells, endothelial cells, and pericytes, whereas neurons were largely depleted (n= 1,777 cells from 2 biological replicates; **Fig. 1f-h, Fig. S1k, Supp. Tables 1-2**). We did not detect robust changes in cell numbers, except for an increase in oligodendrocyte progenitor cells (OPC; **Fig. S3a-b**), as reported previously[31].

Notably, both astrocytes and microglia – but not endothelial or oligodendrocyte lineage cells – showed significant transcriptomic shifts following whisker deprivation (**Fig. 1i**). The astrocytes split into two clusters, one of which (cluster 5) consisted mainly of cells from the control hemisphere, while the other (cluster 1) consisted primarily of deprived cortex. Subclustering and differential gene expression analysis revealed deprivation-induced enrichment for astrocyte genes critical for synapse formation. These genes included *Sparcl1*, which stabilizes nascent synapses[32]. We also identified regulators of cholesterol biosynthesis necessary for synapse formation and glutamate homeostasis (*Cyp51* and *Hmgcs1)*[33–37], and extracellular matrix components and regulators, which contribute to barrel remodeling *(Bcan, Tnc, Htra1*)[38,39] (**Fig. 1j, Fig S3c-e, Supp. Table 3).** We used fluorescent *in situ* hybridization to validate a deprivation-induced increase in *Htra1*, a secreted serine protease which degrades extracellular matrix (**Fig. 1k-l**;[40–43]). Microglial clustering showed a more complex response to remodeling than astrocytes, prompting us to examine them at higher resolution.

A type I interferon-responsive microglial subset expands 20-fold during cortical remapping

Microglia have multiple developmental functions that may be relevant to barrel maturation. They engulf synapses in some developmental and disease contexts[44,45], promote synapse formation, maturation, and plasticity[25,46,47], and engulf dead or dying cells[48–51]. Neuronal cell death in this region peaks at P5-P6 and ongoing synaptic and dendritic formation and remodeling occurs throughout the first postnatal week and beyond[18,52]. To molecularly define this microglial response with additional temporal resolution, we performed single cell RNA sequencing of microglia at P5 and P7 after induction of topographic remapping via whisker removal at P2. We purified microglia using mechanical dissociation followed by magnetic bead isolation, which is ideal for preserving *in vivo* microglia signatures, although it depletes other glial subsets (**Fig. 2a**,[53–57]). We recovered 12,330 cells from 10 mice after quality control and identified 10 microglial clusters. Two pairs of closely related clusters, 0/5 and 6/7, were combined with their nearest neighbors due to low numbers of uniquely enriched genes; of the resulting eight clusters, four were altered by whisker deprivation (**Fig. 2b-e,** quality control in **Fig. S4a-f, Supp. Tables 1, 4-5**). Cell cycle analysis showed that clusters 1, 2, and 6/7 clustered mainly by markers of the different stages of cell division and thus were not examined further (**Fig. S4g-h**). These proliferating clusters were more abundant at P7 than P5 (**Fig. S4i-j**). We also identified a small macrophage subset (1% of cells, cluster 9, *Pf4*, *Lyve1*) that was not substantially changed by whisker deprivation.

We focused on the four non-proliferative clusters of microglia (0/5,3,4,8), which all changed in relative abundance after cortical remodeling. Cluster 0/5, the largest subset, was most similar to homeostatic microglia (*P2ry12, Ccr5*), and decreased modestly after whisker deprivation. The cluster most closely related to cluster 0/5 was cluster 4, which in turn was the most similar to 'proliferative-region associated microglia' (PAMs, 38/42 genes upregulated;[9,10]) and was the only cluster to exhibit modest similarity with 'damage-associated microglia' (DAMS) identified in previous studies[58] (36/83 genes upregulated; **Fig. S4k-l**). Cluster 4 also decreased modestly after whisker deprivation. In contrast, cluster 3 was enriched in canonical neuronal genes (*Rbfox3, Grin1)* and modestly increased after whisker deprivation (**Fig. 2c-d**).

The most striking difference between control and whisker-deprived conditions was the emergence of a microglial subpopulation enriched in type I interferon (IFN-I) response genes (cluster 8). The IFN-I response is a highly evolutionarily conserved antiviral response, but its functions in the developing brain are unknown[59]. Differential gene expression and Gene Ontology (GO) analysis on cluster 8 revealed a robust interferon response signature (*Ifitm3*, *Mx1*, *Ifit3, Isg15*, *Irf7,* and *Stat1)* and GO terms "Response to virus" (GO:0009615), "Response to interferon-alpha" (GO:0035455), and "Response to interferon-beta" (GO:0035458) (**Fig. 2f-g)**. The interferon-responsive cluster 8 was enriched 20-fold in P5 deprived vs. control cortices (0.5% in control vs 11% in deprived) but was indistinguishable from control by P7 (0.6% vs 0.4%) (**Fig. 2h-i, Fig. S4m-p**). This cluster was located between microglia and macrophages in UMAP space but showed microglia-like expression of *Tmem119*, *Tgfbr1*, and *Hexb* (**Fig. S4q**). We observed little to no overlap between this IFN-I responsive cluster and the genes previously described in 'damage-associated microglia' (DAMS, **Fig. S4k**[58]). These data reveal a microglial subset that is rare in the typically developing cortex but expands markedly during a restricted phase of topographic remapping.

The transmembrane protein IFITM3 defines a phagocytic microglial subset enriched during cortical remapping

To further determine whether interferon-responsive microglia represented a *bona fide* microglial subtype *in vivo*, we examined markers that could be used for immunostaining in tissue sections. *Ifitm3* was the most highly upregulated gene in interferon-responsive cluster 8 (**Fig. 2f, Fig. 3a**). This IFN-α/β - stimulated gene encodes a transmembrane protein known to limit viral replication, cancer progression, and amyloid beta plaque deposition[60–63]. We identified a rare population of IFITM3+ microglia in layers 4 and 5 of developing barrel cortex that were increased up to 8-fold during topographic remapping, as quantified *in situ* and by flow cytometry **(Fig. 3b-c; Fig. S5a-d).** We further confirmed that IFITM3+ cells expressed *Mx1*, the canonical interferon stimulated transcription factor also enriched in cluster 8, as assessed by flow cytometry using an $\mathrm{Mx1^{GFP}}$ reporter[64] (**Fig. S5e-f**). An alternate cluster 8 marker, BST2 (a.k.a. Tetherin [65]) was also increased after whisker deprivation and was expressed in most IFITM3+ cells, where it localized to an intracellular compartment (**Fig. S5g-i**). Consistent with its less specific expression in cluster 8 by single cell sequencing (**Fig. S5j**), a portion of BST2+ cells did not co-express IFITM3. Based on the similarities in developmental abundance, induction with barrel remodeling, location near barrels, and its high concordance with two other markers that define our single cell cluster, we conclude that IFITM3 is a sensitive and specific marker that can identify the interferon-responsive cluster 8 *in situ*.

We observed that IFITM3+ microglia were morphologically distinct, with two main subtypes. One type exclusive to layer 4 extended a singular primary process to invade the barrel hollow (‘projecting’), whereas a second type contained prominent IFITM3+ phagocytic cups enveloping DAPI+ nuclei (**Fig. 3d-e**). In contrast, IFITM3- microglia were predominantly ramified. IFITM3+ microglia often contained multiple DAPI+ phagocytic inclusions, which appeared only rarely in IFITM3- microglia (**Fig. 3f-g**). Furthermore, IFITM3+ cells had higher levels of the lysosomal marker CD68, consistent with increased phagolysosomal activity[66] (**Fig. 3h-i**).

Phagocytosis proceeds in stages which include enveloping of extracellular material by the phagocytic cup, packaging into a phagosome, fusion to mature lysosomes to form a phagolysosome, and resolution of the phagolysosome by fragmentation[67,68]. Our data suggested that multiple stages of phagocytosis might be regulated by the interferon stimulated genes expressed in cluster 8. IFITM3+ cells were more likely to contain phagocytic cups than IFITM3- microglia (90% vs. 7%; **Fig. 3j-k**) but were also more likely to contain both early and late stages of phagocytosis in the same cell (**Fig. 3l).** While IFITM3 was enriched around phagocytic cups and diminished with closure of the phagocytic cup and upregulation of CD68+ (**Fig. S5k-l**), BST2 was enriched in a perinuclear compartment (**Fig. S5g**). Whisker deprivation led to a significant increase in the number of microglia with phagocytic cups, phagolysosomes, or both (**Fig. S5m-n)**. Taken together, these data suggest that IFN-I broadly amplifies the microglial phagocytic response, and that IFN-I responsive microglia are enveloping whole cells and often multiple cells simultaneously.

Type I Interferon responsive microglia are poised for neuronal engulfment

Our data suggest that IFN-I responsive microglia are actively engulfing DAPI+ cells. However, the cluster itself was not enriched for traditional phagocytic genes. This prompted us to further examine the dynamic lineage relationships between interferon-responsive cluster 8 and its neighbors. We performed RNA velocity analysis, which uses the ratio of unspliced pre-mRNA to spliced mRNA to infer trajectories between neighboring clusters on the time scale of hours, with higher velocities predicting a faster transition between cell states[69]. Interferon-responsive cluster 8 showed a predicted trajectory towards cluster 3 (**Fig. 4a-b**). Of note, clusters 3 and 8 were both distinct from the predominant cluster linked to lysosomal function, cluster 4 (*Cd68, Trem2, Apoe*; GO:0005764, “lysosome”; **Fig. S6a-b**). From this analysis, we hypothesized that the IFN-I responsive cluster 8 might be functionally linked to cluster 3.

To infer potential functional relationships between the IFN-I responsive cluster and cluster 3, we examined this cluster in further detail. Differential gene expression and ontology showed a marked enrichment in neuronal mRNAs (*Rbfox3, Grin1, Gria1*) (**Fig. 4c-d**), and less commonly other cell type-specific mRNAs, including oligodendrocytes *(Vcan*) and astrocytes (*Sparcl1*; **Fig. S6c**) without any downregulation of canonical microglial genes. Most cells in cluster 3 expressed more neuronal mRNAs than the upper 95th percentile of all other clusters, suggesting that this finding was not due to an outlier effect (**Fig. 4e**). Non-microglial mRNA could indicate an atypical gene expression profile or captured foreign material. Although we cannot rule out the former possibility, we concluded that it was unlikely for two reasons. First, the promoters for these genes were significantly less likely to be accessible relative to promoters of known microglial genes expressed by cluster 4 based on cross-correlation with an ATAC-Seq dataset of cortical microglia **(Fig. S6d-e, Supp. Table 6;** [70]). Secondly, these non-canonical microglial genes in cluster 3 were significantly enriched for intronic sequences associated with unspliced transcripts, relative to canonical microglial genes (**Fig. S6f-g, Supp. Table 7**). These data suggest that the neuronal mRNA observed in nearly all cluster 3 microglia could result from captured foreign mRNA.

We next sought to determine whether a neuron-engulfing microglial subset was present *in situ*. In situ hybridization for *Rbfox1* and *Grin1*, two of the most abundant transcripts in cluster 3, revealed microglia forming phagocytic cups around neuronal soma (**Fig. 4f-g**). Definitive neuron-engulfing phagocytic cups constituted 80% of these engulfing microglia at P5, and 20% at P7, suggesting that when the IFN-I responsive subset is abundant, most engulfed cells were neurons. Once the phagocytic cup closed, these transcripts were undetectable (**Fig. 4f**), as was expression of marker proteins such as NeuN (not shown). We therefore examined microglial engulfment in cell-type specific TdTomato (TdT) reporter lines (*Ai14;* Jax 007908), given this marker's relative stability in the lysosome. In a $Rorb^{cre}$;*R26R-TdT* line labeling most excitatory L4/5 neurons, but not dendrites from other layers ([71]; Jax **023526**), we observed that 9% of L4/5 microglia at P5 had TdT-positive CD68-containing phagolysosomes, suggesting that they had recently engulfed neuronal soma (**Fig. 4h**, **j**). In contrast, we observed no TdT inside microglia in an astrocyte reporter line at this age ($Aldh1l1^{TdT}$; **Fig. 4i-j**). These data suggest that microglia in the barrel cortex engulf neurons *in vivo* after whisker deprivation.

To directly address whether IFN-I responsiveness precedes a neuron-engulfing state, we labeled microglia that had previously expressed *Mx1* using an $Mx1^{Cre}$;*R26R-TdT* reporter (Jax 003556 [72]). Twenty percent of microglia in control cortices at P7 were $Mx1^{TdT}$+ (vs. 1% IFITM3+ cells at P5). This increased to ~50% after deprivation (vs. 12% IFITM3+; **Fig. 4k-l)** indicating that many cells not currently expressing IFITM3 were previously IFN-I-responsive. We next examined whether a history of IFN-I responsiveness predicted whether microglia would contain neuronal mRNA. We found that $Mx1^{cre}$TdT+ microglia were significantly more likely to contain phagocytic cups with *Grin1* mRNA (**Fig. 4m-n**). Taken together, these data are consistent with a model in which the IFN-I response is a transient state that precedes engulfment of neuronal soma.

Type I interferon deficiency leads to dysmorphic microglia with enlarged phagocytic compartments

To determine whether IFN-I signaling impacts microglial phagocytosis and neuronal engulfment *in vivo*, we examined mice lacking the obligate IFN-I receptor *Ifnar1* (Jax 028288; **Fig. 5a**). Microglial IFITM3 expression after whisker deprivation was completely abolished in $Ifnar1^{-/-}$ mice (**Fig. 5b**), confirming that the interferon-responsive microglial subset requires canonical IFN-

I signaling. We found that microglia from *Ifnar1*$^{-/-}$ mice contained markedly enlarged phagocytic compartments with thin walls enclosing diffuse DAPI+ nuclear material (**Fig. 5c-d**). In wild-type microglia these were smaller with condensed DAPI signal that was completely enveloped by the membrane. In *Ifnar1*$^{-/-}$ microglia (**Fig. 5e-f**) and frequently observed multiple phagocytic compartments per cell (**Fig. S7a, Supplemental movie 1)**, reminiscent of 'bubble' microglia observed in zebrafish with deficits in phago-lysosomal fusion[73]. We found that bubble microglia --defined as containing a DAPI+ phagocytic compartment larger than the microglial nucleus -- were rare in control mice, representing 5-15% of microglia in control and deprived cortices respectively. In contrast, up to 40-60% of barrel cortex microglia from *Ifnar1*$^{-/-}$ mice had bubble morphologies (**Fig. 5g-h**). Dysmorphic microglia were also increased in other regions of the *Ifnar1*$^{-/-}$ brain, including the corpus callosum and thalamus (**Fig. S7b-c**.) However, microglial density was unchanged (**Fig. S7d**.) Microglia from *Ifnar1*$^{-/-}$ animals also exhibited an increase in the accumulation of lysotracker, a dye that labels acidic cellular compartments including late endosomes and lysosomes (**Fig. S7e-f**). This increase was closely correlated with the increase in CD68 in both genotypes, suggesting that there was not a significant acidification defect (**Fig. S7g**).Thus, loss of IFN-I signaling results in microglia with an accumulation of enlarged acidified phagolysosomal compartments.

IFN-I signaling restricts the accumulation of damaged neurons

We next examined whether IFN-I deficiency led to broader functional impacts in the developing barrel cortex. As IFN-I responsive microglia were engulfing neurons, we wondered if IFN-I deficiency might lead to an accumulation of dead neurons. Surprisingly, we found that *Ifnar1*$^{-/-}$ mice had a significant decrease in the number of TUNEL+ cells, a label of end stage DNA fragmentation (**Fig. 6a-b**). Furthermore, we found that most TUNEL+ cells (60%) in wild-type mice were completely surrounded by microglia and a minority (20%) lacked any microglial contact. In contrast, TUNEL+ cells in *Ifnar1*$^{-/-}$ mice were much more likely to be found dying alone (**Fig. 6c-d**). A similar deficit in microglial contact was observed with activated Caspase-3+ apoptotic cells (**Fig. S8a-b**). Thus, IFN-I deficiency leads to fewer dead cells and impaired microglial contact with dying cells.

Given the decrease in cells with end-stage DNA fragmentation in the IFN-I deficient cortex, we next examined earlier stages of DNA damage using the marker 53BP1, which accumulates at double-strand DNA (dsDNA) breaks[74,75]. These DNA lesions occur in pathologic and physiologic contexts, including with neuronal activity and during development[76,77]. We observed that cells with dsDNA breaks, which were primarily neurons, increased significantly after whisker deprivation in layer 5 (**Fig. S8c-d**). This suggests that topographic remapping is a developmental stressor that increases neuronal damage. We also found a significant increase in the percentage of cells with dsDNA breaks in the barrel cortex of *Ifnar1*$^{-/-}$ mice relative to wild type littermates (**Fig. 6e-f**), indicating an accumulation of damaged neurons in IFN-I deficient brains.

We further observed that in wild-type mice, microglia with a projecting morphology (as described in **Fig. 3d**) frequently contacted cells with 53BP1+ foci (**Fig. 6g-h**). Consistent with this, we found that IFITM3+ cells were more likely to contact damaged neurons labeled by γH2AX, an independent marker of dsDNA breaks that colocalized with 53BP1 ([78,79] ;**Fig. S8e-g**). To test sufficiency we administered interferon-β (IFN- β) directly into the lateral ventricle and examined 24 hours later. Although the vehicle injection induced an increase in DNA damage over baseline, we were able to observe significant induction of IFITM3+ microglia and a decrease in the accumulation of DNA damage, as IFN- β exposed brains had significantly fewer 53BP1+ puncta per cell (**Fig. S8h-l**). Taken together, these data support a model in which IFN-I responsive microglia promote the elimination of damaged but still viable neurons, a process known as phagoptosis.[80]

To directly visualize the impact of IFN-I signaling on microglial-neuronal interactions, we performed live imaging in zebrafish (*Danio rerio*). This is an ideal model system for imaging the intact developing brain with an evolutionarily conserved antiviral IFN-I system [81,82]. We activated IFN-I signaling four hours prior to imaging with an intraventricular injection of the viral mimic poly(i:c) into zebrafish expressing the myeloid reporter *Tg(mpeg:EGFP-CAAX)* and the pan-neuronal reporter *Tg(NBT:dsRed)* (**Fig. 6i**). We used larvae at 7 days post fertilization, focusing on the optic tectum, which includes a resident population of neuron-engulfing microglia[83,84]. Microglia in vehicle injected fish had a ramified morphology and made frequent passing contacts with neuronal soma, whereas poly(i:c) exposed microglia were markedly more phagocytic (**Fig. 6j**, **Supplemental Movies 2-3).** Poly(i:c) led to a four-fold increase in the percent of microglia engulfing at least one neuron (**Fig. 6k**) and significantly increased the percentage of microglia engulfing multiple neurons over a 30-minute imaging window (**Fig. 6l**), similar to what we observed in IFN-responsive murine microglia after whisker deprivation (**Fig. 3f-g**). We also classified microglial process behaviors (examples in **Fig. S8m**). IFN-I stimulation significantly decreased ramified process motility, while increasing phagocytic cup formation and the enveloping and retraction of neuronal soma (**Fig. 6m-n).** Thus IFN-I is sufficient to induce microglial neuronal engulfment in zebrafish.

Microglia upregulate a conserved interferon-response signature in pathology

To determine if interferon-responsive microglia are unique to this experimental paradigm, we examined murine microglial bulk transcriptomic datasets from a variety of physiological and pathological conditions (**Fig. 7a**, **Supp. Table 8**[85]). As expected, we found the greatest enrichment of the interferon-response signature after viral infection (lymphocytic choriomeningitis, LCMV). However, we also detected prominent induction of an interferon response in various sterile pathologies, including mouse models of brain tumors and of Alzheimer's disease (AD). We found similar results across a variety of single cell datasets including AD models, glioblastoma models, Sars-CoV-2 infection, demyelinating injury (LPC, Cuprizone treatment), aging, and middle cerebral artery occlusion (**Fig. S9a-b, Supp. Table 9**,[9,85–92]).

Type I interferon signaling is one of the first lines of defense against viral infection, and we expected to see IFITM3 upregulated in microglia after viral infection based on canonical signaling and transcriptomic data (**Fig 7a, Fig. S9a-b**,[59]). We examined this *in situ* in a mouse model of SARS-CoV-2 infection, given its major public health interest, known involvement of IFITM3[93–95], and recent reports of potential neurologic sequelae[96–98]. We performed intranasal inoculation of a SARS-CoV-2 strain isolated from a patient into K18-ACE2 transgenic mice, which express the human ACE2 receptor under the cytokeratin-18 (K18) promoter[99–102].

We observed high levels of IFITM3 in most microglia in brains with active viral replication (**Fig. 7b-c**) which was detectable in 2 out of 3 mice at 6 days post infection (DPI) and 0 out of 3 mice at 3 DPI, as assessed by SARS-CoV-2 Spike and N-protein expression **(Fig. 7b-c**; [103,104]) IFITM3 intensity was strongly correlated with infectivity, as assessed by Spike protein intensity (r=0.93, **Fig. 7d-e**). We detected an increase in IFITM3 in both microglia and non-microglial cells, while infected cells were almost exclusively NeuN+ neurons, with highest levels in cortex and hippocampus and undetectable levels in the cerebellum (**Fig. S10a-d**). Microglia expressing higher levels of IFITM3 were also more likely to form phagocytic cups around SARS-CoV-2 Spike+ cells (**Fig. 7d,f, Fig. S10e**) and were more likely to have an amoeboid morphology (**Fig. S10f**).

Type I interferon responses may exacerbate pathology in aging and Alzheimer's disease (AD) [85,86,105–108], thus we examined whether IFITM3+ microglia could also be identified in an AD mouse model *in situ*. We examined 5xFAD mice, characterized by early Aβ deposition and plaque formation followed by decreased performance on cognitive tasks and neuronal loss by 9 months[109]. In 12 month old 5xFAD mice, we observed that 21% of microglia in the ventral hippocampus were IFITM3+, whereas few were detected in aged-matched controls (**Fig. 7g-h**). We also detected IFITM3 in astrocytes as previously described[60], which was ubiquitous throughout the hippocampus in both control and 5xFAD settings and enriched in a GFAP+ cytoskeletal pattern. IFITM3+ microglia were significantly more likely to be associated with amyloid plaques than IFITM3- microglia and were twice as likely to contain at least one phagocytic cup (**Fig. 7i-j**). As in the developing cortex, these phagocytic cups were enriched for IFITM3 protein (**Fig. 7g, k**). We observed a positive correlation between IFITM3 levels within phagocytic cups and the amount of engulfed Aβ (**Fig. 7k-l**), although we did not observe phagocytic cups around neuronal soma at this time point. These data indicate that IFN-I responsive microglia are present in the model. However, as Aβ phagocytosis is molecularly distinct from whole cell engulfment[110–113], the functional impact of IFN-I responsive microglia in this context remains to be determined. For example, they could play a distinct phagocytic role, such as limiting plaque deposition[114,115], or alternately their induction could lead to a bystander effect that exacerbates neuronal loss.

Discussion

This study defines a coordinated set of functional state changes in microglia in response to developmental barrel cortex remodeling. We identified an interferon-responsive, highly phagocytic population that emerged transiently in microglia during topographic remapping and was required for effective neuronal engulfment during development. IFN-I responses are a central component of antiviral defense, and have been linked to phagocytosis in some pathogenic contexts, but their role in physiology is comparatively unknown[116–119]. The IFN-I responsive microglial subset characterized here is rare but detectable in the normally developing cortex, yet up to 40%

of microglia are dysmorphic in mice lacking IFNAR1, suggesting that IFN-I microglia are rare not because they are dispensable but because they represent a highly transient microglial state. The observation that IFN-I responsive microglia are frequently digesting one cell while in the process of enclosing another, along with the characteristic 'bubble' phenotype of multiple phagosomes per cell in IFN-I deficiency, strongly suggests that IFN-I signaling accelerates phagocytosis in settings where cell turnover is high.

Our data reveals that intact IFN-I signaling in the developing brain optimizes the efficient elimination of damaged neurons. Many outstanding questions remain, including which cells release IFN-α/β, what signals drive microglia to engulf specific cells, and whether cells are eaten dead or alive[49,80,120,121]. Transcriptomic data suggests that microglia themselves could be a source of IFN-β[122]. One potential model is that exposure to damage associated molecular patterns (DAMPs) from stressed cells[48,123] triggers conserved responses adapted to detect nucleic acids[124–127], triggering an autocrine loop which enhances phagocytic efficiency via IFN- α/β release. In this model, physiological and self-contained engulfment events could become pathological if high IFN-I tone or abundant nucleic acids trigger a more widespread microglial response and lead to indiscriminate cell death and neuroinflammation.

Consistent with this proposed model, our data reveal the expansion of an IFN-I responsive microglial subset in pathology. While an IFN-I response is expected during neurotropic viral infection, as we observed in a SARS-CoV-2 model, the association of interferon-responsive microglia with virally infected neurons could prompt further inquiry into potential pathogenic mechanisms. Given emerging reports of neuropsychiatric sequelae following COVID-19 infection in humans[96,98], defining whether this microglial subset is present in human samples or in other animal models may be fruitful[128–130]. Furthermore, we characterize a distinct interferon-responsive microglial subset *in situ* that associates with Aβ plaques in the 5xFAD model of Alzheimer's disease. This is consistent with multiple reports of IFN-I involvement in aging and Alzheimer's disease [60,86,105,106,131,132], and suggests potential roles for an IFN-I induced cell state in regulating Aβ deposition. Abundant IFITM3 staining in other cell types including astrocytes points to a coordinated role of IFN-I signaling in response to widespread cellular stress or damage[106,133]. Ultimately, determining the context-specific mechanisms of microglial engulfment will enable therapeutics to target aspects of phagocytosis while preserving microglial homeostatic function.

Figures

Figure 1: Microglia and astrocytes alter their transcriptomes in response to cortical remapping.

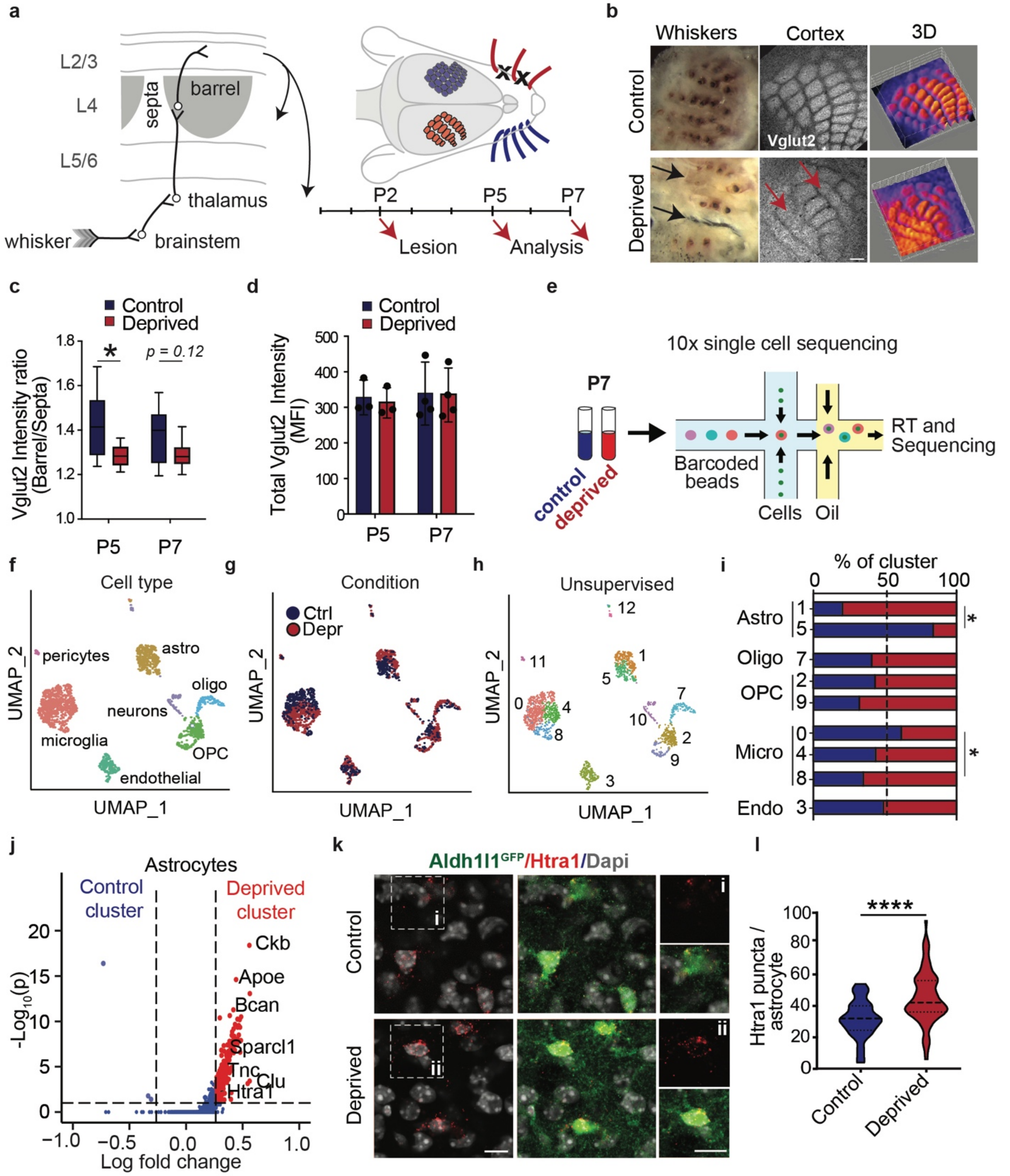

a) Schematic of barrel cortex connectivity and experimental timeline.

b) Representative images of control and whisker lesioned whisker pad (Left), *en face* imaging of L4 somatosensory cortex and cortex topographical heat map derived from VGLUT2 intensity data (right). (Scale bar = 100 µm).

c) Quantification of barrel distinctness based on VGLUT2 intensity in barrels vs. septa in control and deprived hemispheres. Box and whisker plots show range (whiskers), median, and first and third quartiles (box). (2-4 barrel/septa pairs per condition per mouse; P5: n=3 mice, P7: n=4 mice, 2-way ANOVA with Sidak post-hoc test).
d) VGLUT2 intensity averaged over the entire barrel field in the deprived and spared hemispheres. Error bars show mean ± SD. (P5: n=3 mice, P7: n=4, 2-way RM ANOVA with Sidak post-hoc test).
e) Schematic of single cell barcoding and RNA sequencing using the 10x Chromium system.
f) UMAP plot of non-neuronal single cell sequencing in P7 barrel cortex labelled by cell type assigned by representative marker analysis.
g-h) Data in F plotted as control vs. whisker deprived hemisphere (**g**) and unsupervised clustering (**h**).
i) Percent of each cluster in control (blue) vs. deprived (red) hemispheres. (Chi-square test, * p<0.01, f > 0.15).
j) Differentially expressed genes between the astrocyte cluster 1 (deprived-enriched) and astrocyte cluster 5 (control-enriched.) Significance: enriched > 30%, adjusted p-value < 0.001.
k) Representative image of quantitative in situ hybridization for *Htra1* mRNA co-stained with Aldh1L1-GFP astrocyte reporter. Inset highlights a single astrocyte. (Scale bar = 10 µm)
l) *Htra1* mRNA puncta per astrocyte in control and deprived hemispheres. (n= 65 astrocytes (control) and 82 astrocytes (deprived) from n=3 mice, Welch's t-test).
*Statistics: All tests shown are two-tailed. *p<0.05, **p<0.01, ***p<0.001, ****p<0.0001 unless otherwise noted. Graphs shown as mean ± SD (bar graphs) or mean ± SEM (stacked bar graphs).*

See also Figures S1-S3, Supplementary Tables 1-3

Figure 2. A type I interferon-responsive microglial subset expands 20-fold during cortical remapping.

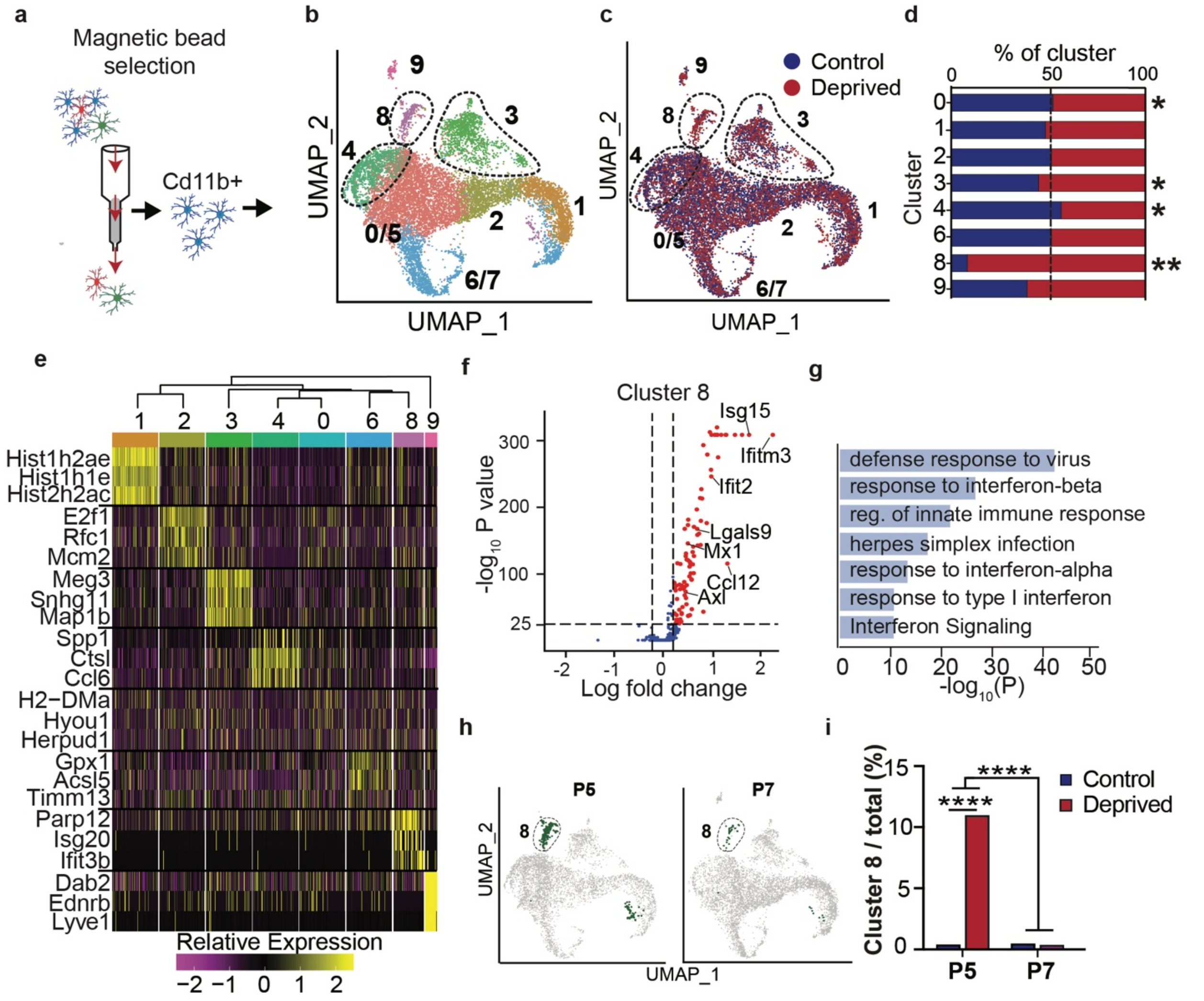

a) Schematic of MACS-isolation of microglia for single cell sequencing.

b) UMAP plot showing independent clustering of 12,000 CD11b+ cells, pooling P5 and P7 timepoints from control and whisker deprived cortices, including microglia (Clusters 0- 8) and macrophages (Cluster 9). Dotted lines highlight clusters for further analysis. Clusters 0/5 and 6/7 were the results of merging nearest neighbor clusters 0 and 5 as well as 6 and 7 due to low numbers of uniquely expressed genes.

c) Clusters colored by condition (control vs. whisker deprived).

d) Quantification of cluster composition by condition. X-axis represents percent of cells in each cluster from the control (blue) or deprived (red) hemispheres, normalized for total number of cells per sample. (Chi-square test with Bonferroni correction, * $p_{Adj} < 0.01$, ** $p_{Adj} < 10^{-25}$).

e) Heatmap of top differentially expressed genes (log$_2$ fold change, $p_{Adj} < 10^{-25}$).

f) Volcano plot of genes differentially expressed in cluster 8 relative to all other clusters.

g) Cluster 8 upregulated GO terms.

h) Clusters separated by age (P5 vs. P7) with cluster 8 highlighted (green).

i) Plot of cluster 8 abundance at each time point in control vs. deprived conditions (Chi-square test with Bonferroni correction, **** $p_{Adj} < 10^{-10}$).

See also Figure S4, Supplementary Tables 4-5.

Figure 3. The transmembrane protein IFITM3 defines a phagocytic microglial subset enriched during cortical remapping.

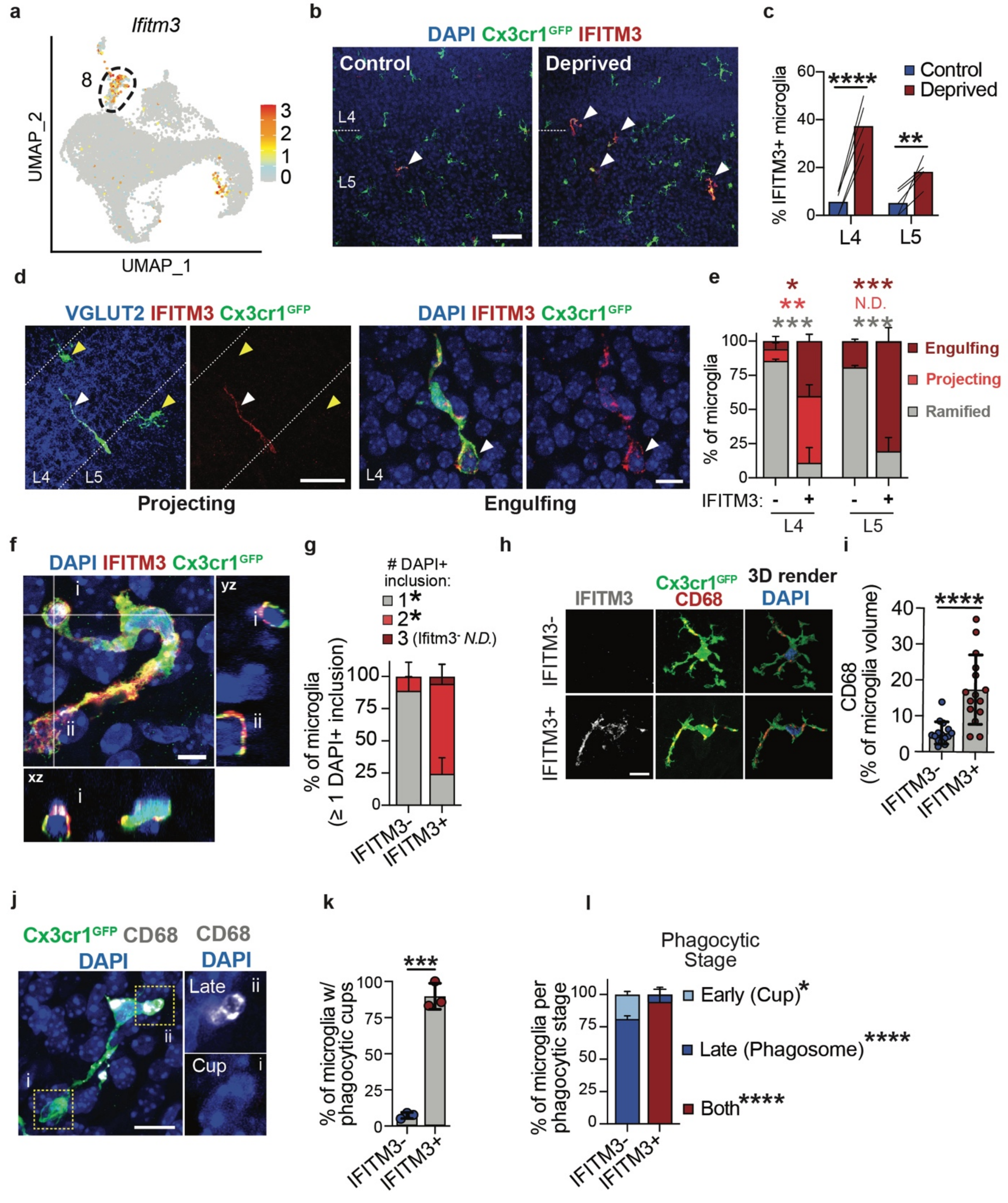

a) UMAP feature plot showing normalized expression of cluster 8 marker gene *Ifitm3*.

b) Representative image of IFITM3+ microglia (arrowheads) in control or whisker-deprived somatosensory cortex at P5 (Scale = 50 μm).

c) Percent IFITM3+ microglia in coronal sections from layers 4 and 5 (L4, L5). Lines connect control and deprived from the same mouse (n=5, 2-way RM ANOVA with Sidak post-hoc test).

d) Representative image of 'projecting' and 'engulfing' IFITM3+ microglia in P5 deprived cortex (Coronal sections, scale = 20 µm (left), 5 µm, (right)).
e) Quantification of microglial morphological subtypes described in **e** (n = 4 mice, 2-way RM ANOVA with Sidak post-hoc test).
f) Confocal image and orthogonal views of an IFITM3+ microglia containing multiple phagocytic cups (i, ii show nuclei-containing phagocytic cups that are distinct from the microglia nucleus). (Scale bar = 5 µm)
g) Number of DAPI+ phagocytic compartments (inclusions) per microglia, among microglia with at least one DAPI+ phagocytic compartment (n = 4 mice, 2-way RM ANOVA with Sidak post-hoc test).
h) Representative images and 3D-rendering of CD68+ lysosomes within IFITM3+ and IFITM3- microglia in L4. (Scale = 10 µm)
i) Quantification of % CD68 volume of total microglial volume in IFITM3+ and IFITM3- microglia (13 IFITM3- and 15 IFITM3+ from n= 3 mice, Mann-Whitney test).
j) Representative image of a Cx3cr1-GFP+ microglia highlighting a phagocytic cup (i; $CD68^-$, non-pyknotic DAPI signal, incomplete DAPI envelopment by microglial processes) and a late phagosome or phagolysosome (ii; $CD68^+$, pyknotic DAPI signal, complete envelopment by microglial processes). (Scale bar = 10 µm).
k) Percent of IFITM3- and IFITM3+ microglia containing phagocytic cups. (n = 3 mice, Welch's t-test).
l) Distribution of early phagocytic cups and late phagosomes as a proportion, in microglia containing at least one phagosome. (n = 7-10 cells each from 3 mice/group, 2-way RM ANOVA with Sidak post-hoc test).

*Statistics: All tests shown are two-tailed. *p<0.05, **p<0.01, ***p<0.001, ****p<0.0001 unless otherwise noted. Graphs shown as mean ± SD (bar graphs) or mean ± SEM (stacked bar graphs).*

See also Figure S5.

Figure 4. Type I Interferon-responsive microglia are poised for neuronal engulfment.

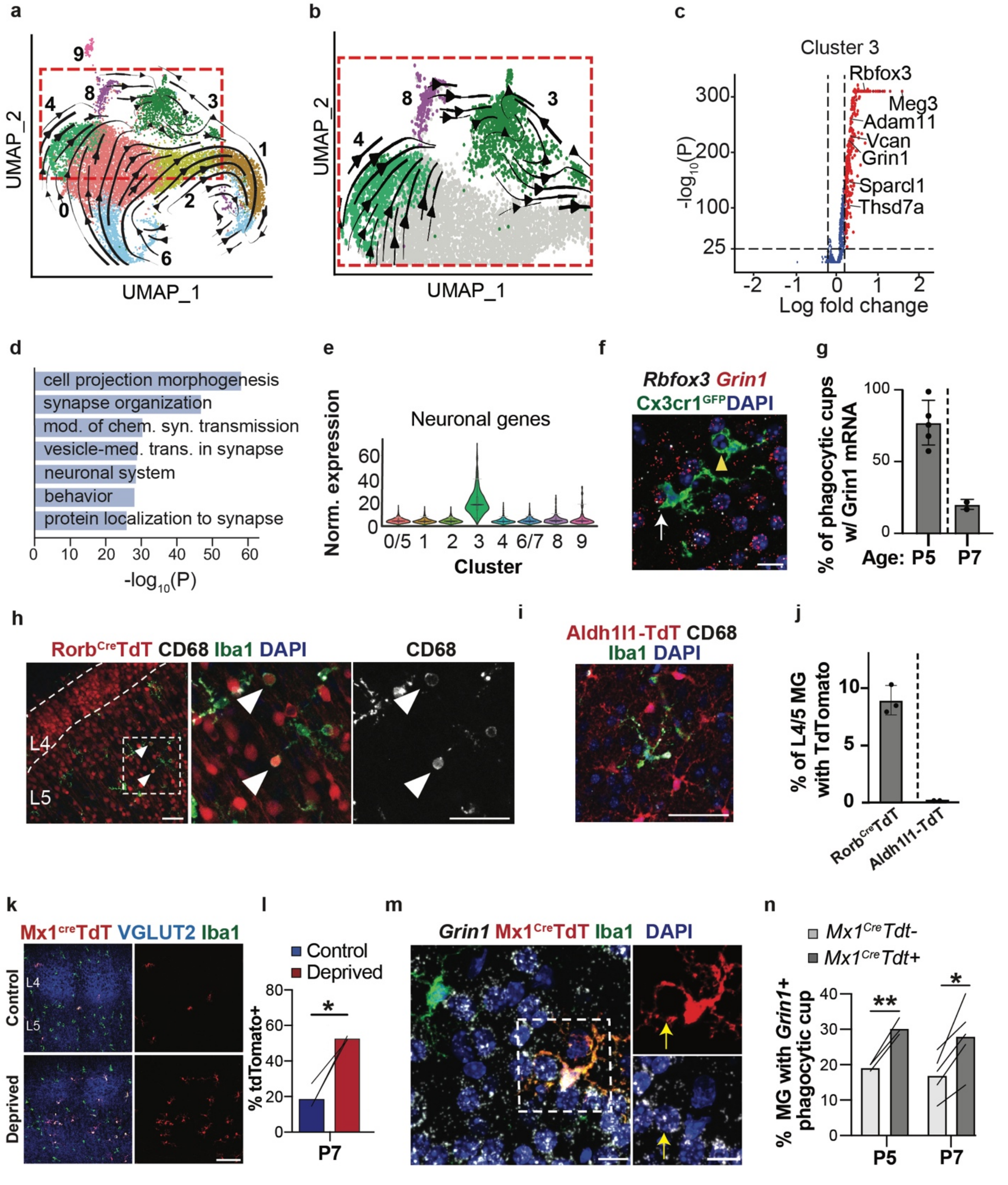

a-b) RNA velocity analysis colored by cluster (scVelo, [69]); Inset highlights clusters 3, 4, and 8.

c-d) Differentially expressed genes and upregulated GO terms for Cluster 3**.**

e) Normalized expression of a neuronal eigengene across clusters numbered as in 2b. The 45 differentially expressed genes in cluster 3 (natural log fold change > 0.25, adj. p < 1e-10) that were neuron-specific (per [122]) were used to define the eigengene. Lines show 5th, 50th, and 95th percentiles.**)**

f) Representative image of neuronal mRNA transcripts *Rbfox3* and *Grin1* in tissues from a Cx3cr1^{GFP} reporter line.

White arrow: a microglial phagocytic cup. Yellow arrowhead: enclosed phagosome lacking neuronal transcripts. (scale bar = 10 µm).
g) Quantifications of percent of phagocytic cups enveloping nuclei with *Grin1* transcripts at the specified ages. Dots=mice.
h) Representative image of Iba1+ microglia engulfing *RorbCre;Ai14*+ neurons in barrel cortex. Inset: layer 5. Arrowheads: Rorb^{cre}TdT positive and CD68+ phagolysosomes. (Scale bar =50 µm) . n=3 mice (Rorb^{Cre}Tdt), 2 mice (Aldh1l1-TdT)
i) Representative image of Iba1+ microglia and Aldh11L1-TdT+ astrocytes in barrel cortex. (scale bar = 50 µm).
j) Quantification of percent microglia containing TdTomato signal in Rorb^{cre}:TdT or Aldh1l1^{TdT} transgenic mice (dots=mice).
k) Representative images of TdTomato+ cells (*Mx1-Cre;Rosa26-LSL-TdT*) in layers 4-5 of barrel cortex co-labeled with microglial marker Iba1 and VGLUT2 to highlight barrels. (Scale bar= 100 µm)
l) TdTomato+ microglia in control and deprived cortices. (n = 3, paired per mouse, paired t-test).
m) Representative image of a Mx1^{cre}TdT + microglial phagocytic cup around a *Grin1*+ nucleus (inset, arrow). (Scale bar =10 µm)
n) Quantification of percent Mx1^{cre}TdT + or negative microglia forming phagocytic cups around *Grin1*+ nuclei. (Scale bar = 10 µm). (n=3 mice at P5 and 5 mice at P7, 2-way RM ANOVA with Sidak post-hoc test).

Statistics: Thresholds in **a, b, c, d** are $p_{adj} < 10^{-25}$ >, natural log fold change > 0.2. *All tests shown are two-tailed.*
**p<0.05, **p<0.01, ***p<0.001, ****p<0.0001 unless otherwise noted.*
Graphs shown as mean ± SD (bar graphs) or mean ± SEM (stacked bar graphs).

See also Figure S6 and Supplementary Tables 6-7

Figure 5: Type I interferon deficiency leads to dysmorphic microglia with enlarged phagocytic compartments.

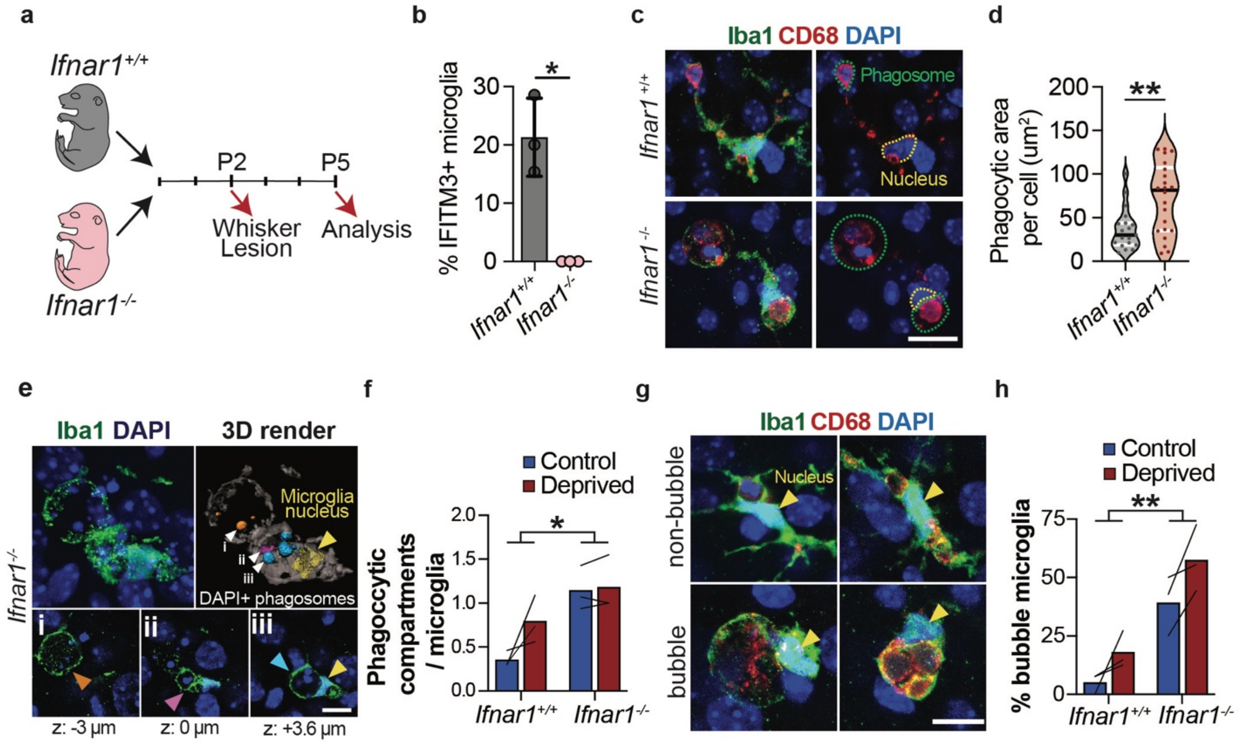

a) Diagram of experimental design comparing control (*Ifnar1*$^{+/+}$) vs. IFN-I insensitive (*Ifnar1*$^{-/-}$) mice.
b) IFITM3+ microglia in deprived hemispheres (L4-5 barrel cortex) from *Ifnar1*$^{+/+}$ and *Ifnar1*$^{-/-}$ (n = 3 mice, Welch's t-test).
c) Representative image of microglia from *Ifnar1*$^{+/+}$ and *Ifnar1*$^{-/-}$ mice. (yellow: microglial nucleus, green: phagocytic compartment, Scale = 15 µm)
d) Total area of phagocytic compartments per microglia in barrel cortex from *Ifnar1*$^{+/+}$ and *Ifnar1*$^{-/-}$ mice. (dots = microglia, n = 3 mice per genotype, Mann-Whitney test).
e) Representative image and 3D render of microglia with multiple phagocytic compartments in *Ifnar1*$^{-/-}$ mouse (White arrowheads: DAPI+ phagosomes; Yellow: microglial nucleus). Insets: cross sections through each phagosome, colored as in render (Scale bar = 10 µm).
f) Phagocytic compartments per microglia in control and deprived cortices from *Ifnar1*$^{+/+}$ and *Ifnar1*$^{-}$ mice. (Lines connect control and deprived hemispheres from individual mice, n = 3 mice/ genotype, 2-way RM ANOVA).
g) Representative images of "bubble" microglia with rounded phagosomes larger than the microglia nucleus (Scale = 10 µm)
h) Percent microglia with bubble morphology in control and deprived barrel cortices from *Ifnar1*$^{+/+}$ and *Ifnar1*$^{-/-}$ mice (n = 3 mice per genotype, 2-way RM ANOVA).
*Statistics: All tests shown are two-tailed. *p<0.05, **p<0.01, ***p<0.001, ****p<0.0001 unless otherwise noted. Graphs shown as mean ± SD (bar graphs) or mean ± SEM (stacked bar graphs).*

See also Figure S7 and Supplemental movie 1.

Figure 6: IFN-I signaling restricts the accumulation of damaged neurons.

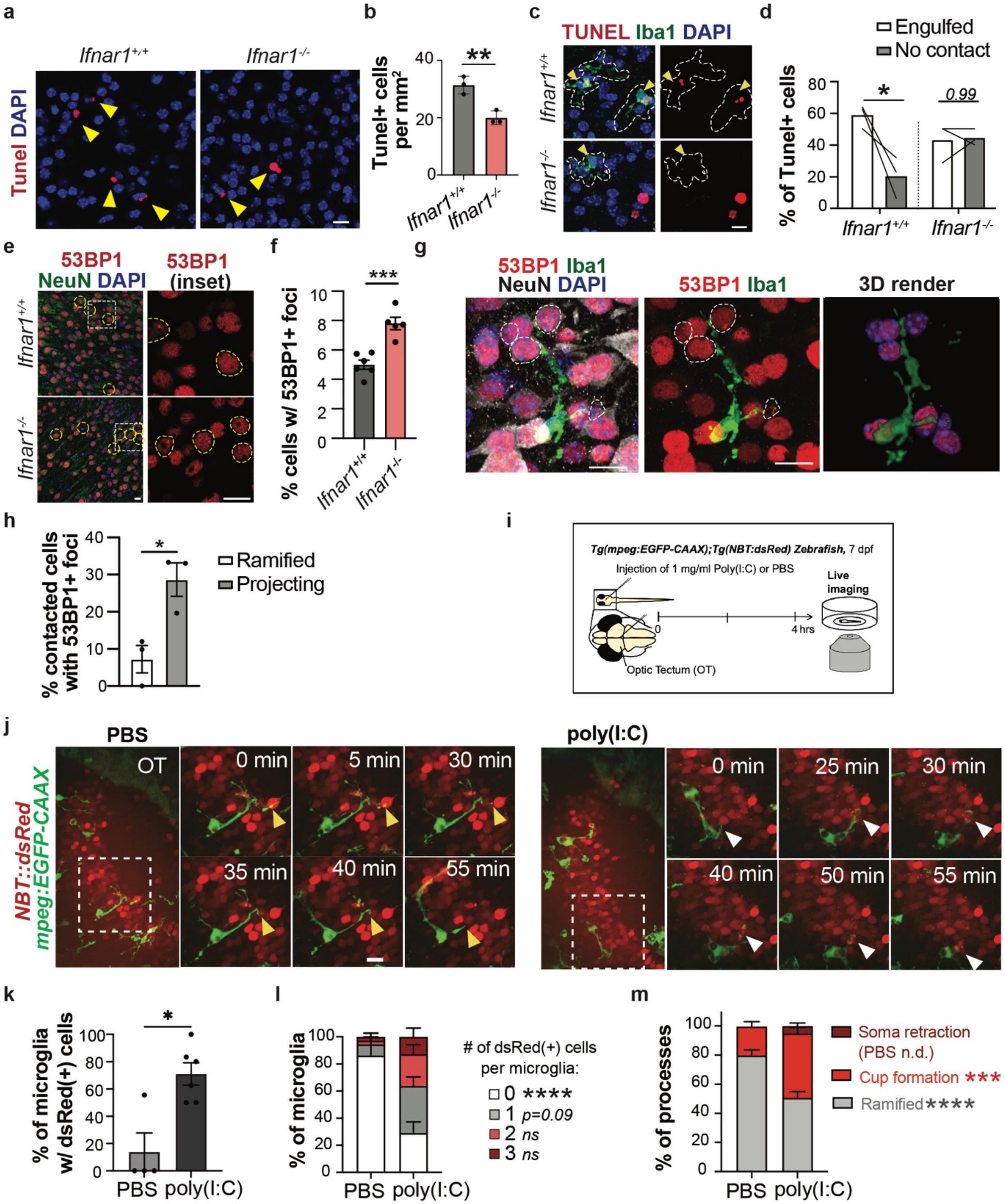

a) Representative image of TUNEL staining in the barrel cortex of *Ifnar1*$^{+/+}$ and *Ifnar1*$^{-/-}$ mice. Arrowheads highlight TUNEL+ cells. (Scale bar = 10 μm).
b) Quantification of TUNEL+ cells in layers 4-5 of the barrel cortex (n=3 mice per genotype, t-test).
c) Representative images of TUNEL+ cells with Iba1+ microglia. Dotted lines outline individual microglia (Scale = 10 μm).

d) Quantification of TUNEL signal inside microglia (“engulfed”) vs outside “no contact”). Yellow arrowhead indicates microglial nucleus, which is distinct from TUNEL signal and non-pyknotic. (n = 3 mice per genotype, 2-way RM ANOVA with Sidak post-hoc test).

e) 53BP1+ neurons in barrel cortices of *Ifnar1*$^{+/+}$ and *Ifnar1*$^{-/-}$ littermates. Yellow dotted lines outline nuclei with 53BP1+ foci, square inset highlights 53BP1staining. (Scale= 10 μm).

f) Percent of all cells in layer 4 containing foci in *Ifnar1*$^{+/+}$ and *Ifnar1*$^{-/-}$ mice (n=6 *Ifnar1*$^{+/+}$and 5 *Ifnar1*$^{-/-}$ mice, t-test).

g) Representative image showing contact between a projecting microglia and 53BP1+ foci-containing neuron. White dotted lines outline nuclei with 53BP1+ foci. 3D render (right), isolates only nuclei (blue) in contact with the microglia (green). (Scale = 10 μm)

h) Percent of cells with 53BP1+ foci in contact with ramified or projecting microglia (dots=mice, 2-3cells/mouse, t-test).

i) Diagram showing parameters for zebrafish poly(i:c) injection and live imaging experiment.

j) Still image (left) and insets showing individual frames (0-55 minutes, region shown by white dotted rectangle) from live imaging of green microglia(*Tg(mpeg:EGFP-CAAX))* and red neurons (*Tg(NBT:dsRed)*) in the zebrafish optic tectum after intraventricular injection of PBS (top) or poly(I:C) to induce an interferon response. The yellow arrowhead shows a single neuron that is contacted by a microglial process but not engulfed. The white arrowhead shows a neuron that is contacted, engulfed, and trafficked towards the microglial soma. (Scale bar = 10 μm).

k) Quantification showing the percent of microglia engulfing at least one dsRed+ cell during the hour-long video. Each dot represents one fish. (n= 4 PBS, 6 poly(I:C), Mann-Whitney test).

l) Quantification showing the percent of microglia engulfing 0, 1, 2, or 3 dsRed+ cells during image acquisition. (n = 4 PBS, 6 poly(I:C), 2-way ANOVA with Sidak post-hoc test).

m) Percent of microglial processes with each of three morphologies (examples are shown in fig. S8). (n = 4 PBS, 6 poly(I:C), 2-way ANOVA with Sidak post-hoc test).

*Statistics: All tests shown are two-tailed. *p<0.05, **p<0.01, ***p<0.001, ****p<0.0001 unless otherwise noted. Graphs shown as mean ± SD (bar graphs) or mean ± SEM (stacked bar graphs).*

See also Figure S8 and Supplemental Movies 2-3.

Figure 7: Microglia upregulate a conserved interferon-response signature in pathology.

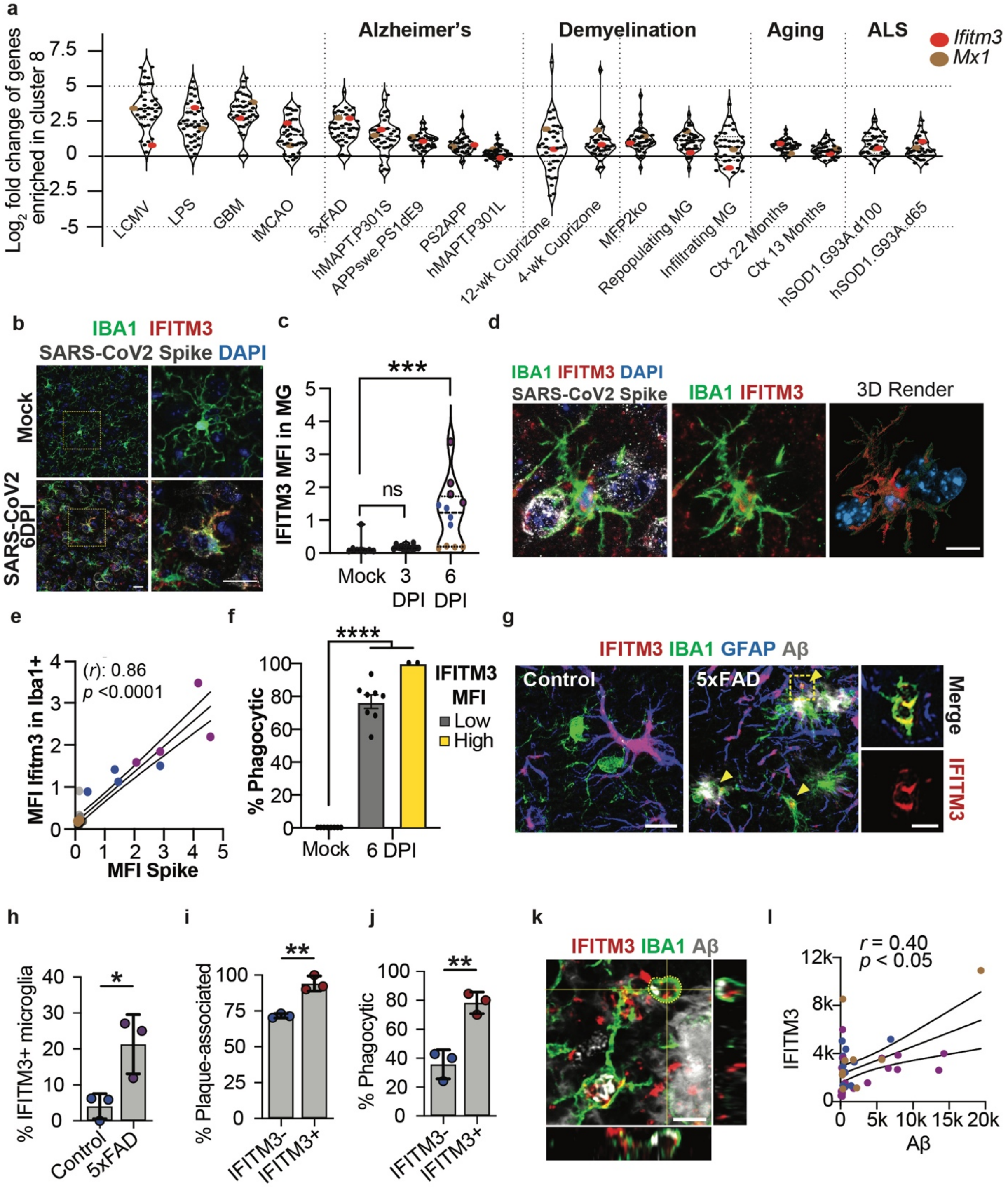

a) Expression of 38 'cluster 8' marker genes across a set of published microglia sequencing data (from bulk sorted CD11b+ cells[85]. Dots represent individual genes, highlighting *Ifitm3* (red) and *Mx1* (orange). y-axis represents the log-fold-change relative to the control in that dataset. See Supplementary Table 7 for details of each sample set and experimental condition.

b) Representative images in somatosensory cortex showing IFITM3 staining in Iba1+ microglia from mock vs. SARS-CoV-2 infected mice 6 days post infection (DPI) (left: low power, right: inset, single microglia, Scale bar = 20 μm).

c) Quantification of IFITM3 mean fluorescence intensity within microglia. Each color represents an individual mouse. (n=2 mock-infected mice, 3 each at 3 and 6 days post infection, Kruskal-Wallis test).
d) Representative image and 3D reconstruction of an IFITM3+ microglia engulfing a SARS-CoV-2 infected cell. (Scale= 10 µm).
e) Correlation of SARS-CoV-2 Spike protein vs. microglial IFITM3 per field of view. Colored by mouse (n = 3 mice at 6 DPI, r = Spearman correlation coefficient).
f) Percent phagocytic microglia in cortices of mock-infected vs. SARS-CoV-2 infected mice at 6 dpi, binned by IFITM3 expression per cell (see Methods for details). (Dots are fields of view from n = 2 mice/group, Kruskal-Wallis test).
g) Representative images of microglia in hippocampi of 12-month old 5xFAD and age matched control mice, labeled with IFITM3, microglia (IBA1), astrocyte (GFAP), and Aβ (FSB dye). Inset: the plaque-adjacent phagocytic cup outlined in yellow.
h) Percent IFITM3+ microglia in 5xFAD and control hippocampi. (n = 3 mice per group, t-test)
i) Percent of microglia in IFITM3+ and IFITM3- populations within 10 µm of an Aβ plaque (n = 3 mice, t-test).
j) Percent of microglia in IFITM3+ and IFITM3- populations containing a phagocytic compartment (n = 3 mice, t-test).
k) Confocal image and orthogonal projection of a plaque-associated IFITM3+ microglia with an Aβ+ (4G8 antibody) IFITM3+ phagocytic cup. (Scale bar = 5 µm).
l) Correlation of Aβ and IFITM3 mean fluorescence intensity per phagocytic compartment. (Colored per mouse, r = Spearman correlation coefficient).
*Statistics: All tests shown are two-tailed. *p<0.05, **p<0.01, ***p<0.001, ****p<0.0001 unless otherwise noted. Graphs shown as mean ± SD (bar graphs) or mean ± SEM (stacked bar graphs).*

See also Figures S9-S10, Supplemental Tables 8-9.

Supplemental movie 1: Imaris reconstructed video scanning through the z-axis of a dysmorphic bubble microglia shown in figure 5e. Green = Iba1 (microglia), blue = Dapi (nucleus), red = CD68 (lysosomes).

Supplemental movies 2-3: Representative live imaging videos of microglia (*Tg(mpeg:EGFP-CAAX))* and neurons (*Tg(NBT:dsRed)*), from vehicle injected (Supplemental movie 2) or polyI:C injected (supplemental movie 3) Each frame consists of one 50 µm z-stack acquired once every 5 minutes, and each video was acquired over one hour.

Table S1: Sample sizes and cell yields from the single cell sequencing in Figures 1 and 2,4.

Sample age	**Sample description**	**#cells after QC**
Pan glial RNAseq (isolated by cold protease digestion), Figure 1		
P7	1 Female, control and deprived hemispheres	394 control, 535 deprived
P7	1 Male, control and deprived hemispheres	276 control , 456 deprived
Microglial only RNA seq (isolated by dounce homogenization), Figures 2, 4		
P5	3 Females, pooled, control and deprived hemispheres	1360 control , 1265 deprived
P5	3 Male, pooled, control and deprived hemispheres	1595 control , 1290 deprived
P7	3, Females pooled, control and deprived hemispheres	2929 control, 2224 deprived
P7	1 Male, control and deprived hemispheres	1165 control , 502 deprived

Table S2 (excel file): Differential gene expression analysis for P7 pan glial single cell sequencing clustering shown in figure 1h.

Table S3 (excel file): Differential gene expression analysis for P7 astrocyte single cell sequencing, comparing deprived-enriched cluster 1 to control-enriched cluster 5, see figure 1j.

Table S4(excel file): Differentially expressed genes for CD11b+ single-cell sequencing clustering shown in Figure 4c.

Table S5 (excel file): Differential expression analysis for in-silico sorted macrophages isolated at P5 and P7, see also figures 2b, e,f,g, 4c, S6a-b.

Table S6 (excel file): Atac-Seq analysis on bulk sequenced microglia isolated by dounce homogenization from a P30 mouse brain, as shown in figures S6d-e.[70]

Table S7 (excel file): Ratio of spliced to unspliced transcripts identified per gene calculated using velocyto and scvelo on the P5/P7 microglial single cell RNAseq dataset. See figure S6g.

Table S8 (excel file): Extended legend for figure 7a including references for all publicly available bulk microglial sequencing datasets used. Table adapted from Friedman et al 2018, figure 4.[85]

Table S9 (excel file): Extended legend for figure S9a-b, including references for all publicly available published single cell sequencing datasets used.

Table S10 (excel file): Summary of statistical analyses.

Supplemental Figure 1: Synapse numbers, glial numbers and glial reactivity are unchanged after partial whisker deprivation.

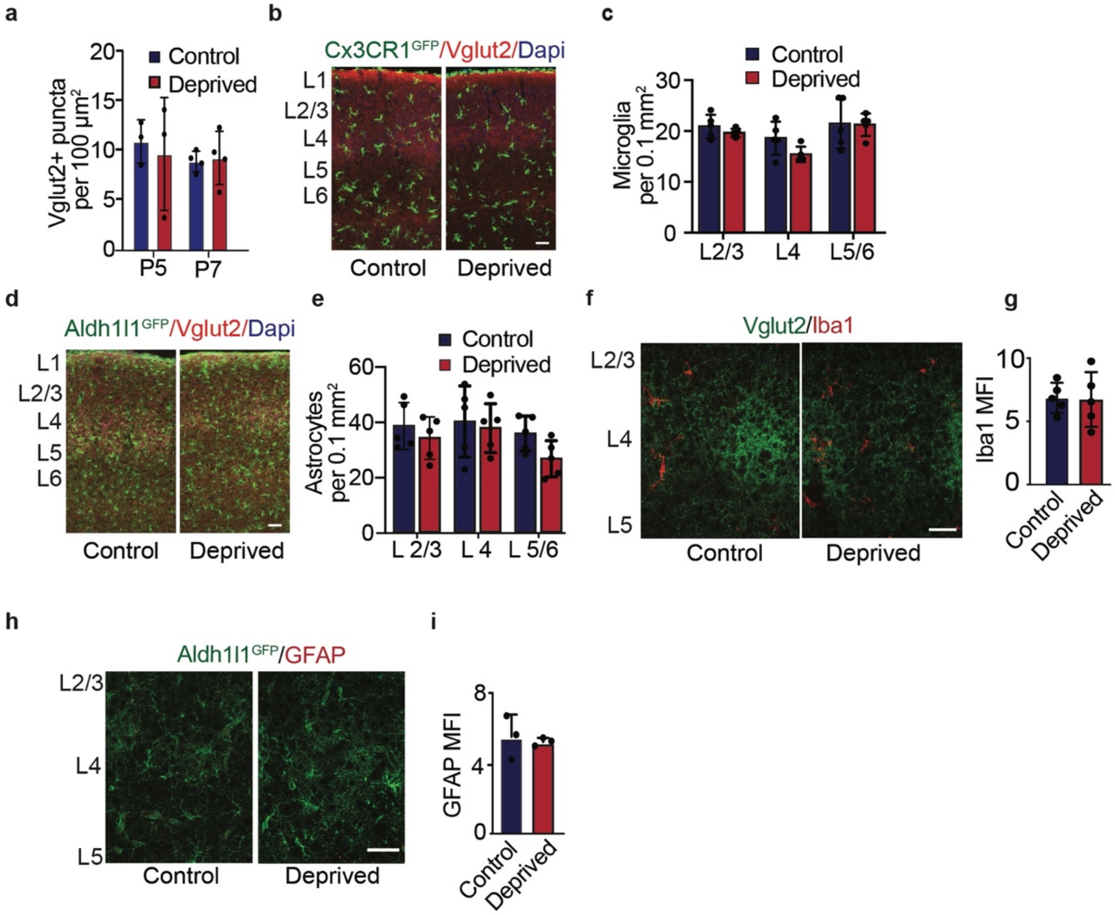

a) Data in Fig. 1D represented as # of VGLUT2+ puncta in barrel cortex after whisker deprivation. (P5: n=3, P7: n=4).
b) Representative image of microglia (Cx3cr1-GFP+) in P7 cortex (Scale bar = 20 μm)
c) Microglial density across cortical layers (n = 4 mice).
d) Representative images of astrocytes (Aldh1l1-GFP+) in P7 cortex. (Scale bar = 20 μm)
e) Astrocyte density across cortical layers. (n = 5 mice).
f-g) Representative images and quantification of Iba1 intensity in coronal sections through the barrel cortex at P7. (Scale bar = 25 μm;n = 28 images from 5 mice).
h-i) Representative images and quantification of with GFAP intensity in Aldh1l1-eGFP+ astrocytes in coronal sections through the mouse barrel cortex. (Scale bar = 25 μm; n = 3 mice).
All error bars show mean ± SD.

Supplemental Figure 2: Optimization of cold-protease digestion strategy and quality control of scRNAseq data in Figure 1.

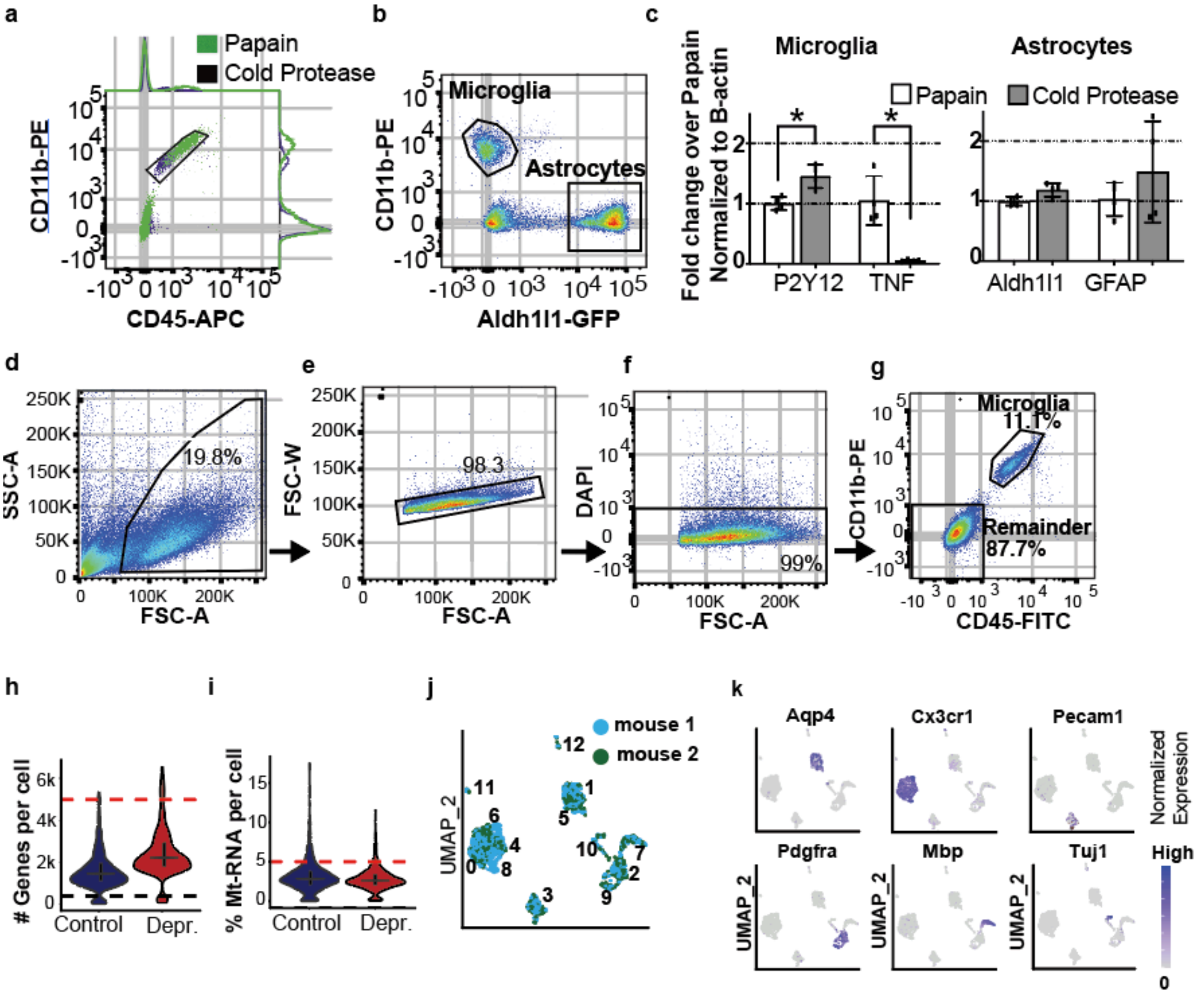

a) Flow gates showing reduced microglial CD45 and CD11b after cold protease digestion at 4° C relative to papain digestion at 34° C.

b) Partial gating strategy for Fig. 1 showing astrocyte and microglia isolation by Fluorescence Activated Cell Sorting (FACS).

c) Representative homeostatic and reactivity markers in microglia and astrocytes after enzymatic dissociation at 34° C (Papain) or 4° C (Cold Proteases), quantitative real time PCR (n=4 mice, Welch's ANOVA with Dunnett's T3 post-hoc test).

d-g) Full gating strategy for live single cell and microglial enrichment. Gating in **g** used to enrich microglia to 30% of total cells.

h-i) Quality control metrics for single cell sequencing showing number of genes recovered and mitochondrial RNA content per cell by sample. Lines show thresholds used for cell selection. Median and 1st and 3rd quartiles shown in black on each violin.

j) UMAP plot colored by biological replicate shows consistency across replicates.

k) Representative feature plots showing genes used for cell type classification, including *Cx3cr1* (Microglia), *Aqp4* (Astrocytes), *Pecam1* (Endothelial cells, CD31), *Pdgfra* (OPCs), *Mbp* (Oligodendrocytes), and *Tubb3* (Neurons, TUJ1).

*Statistics: All tests shown are two-tailed. *p<0.05, **p<0.01, ***p<0.001, ****p<0.0001 unless otherwise noted. Graphs shown as mean ± SD (bar graphs) or mean ± SEM (stacked bar graphs).*

Supplemental Figure 3: Additional analyses of oligodendrocyte progenitor cells and astrocytes in barrel cortex after whisker deprivation.

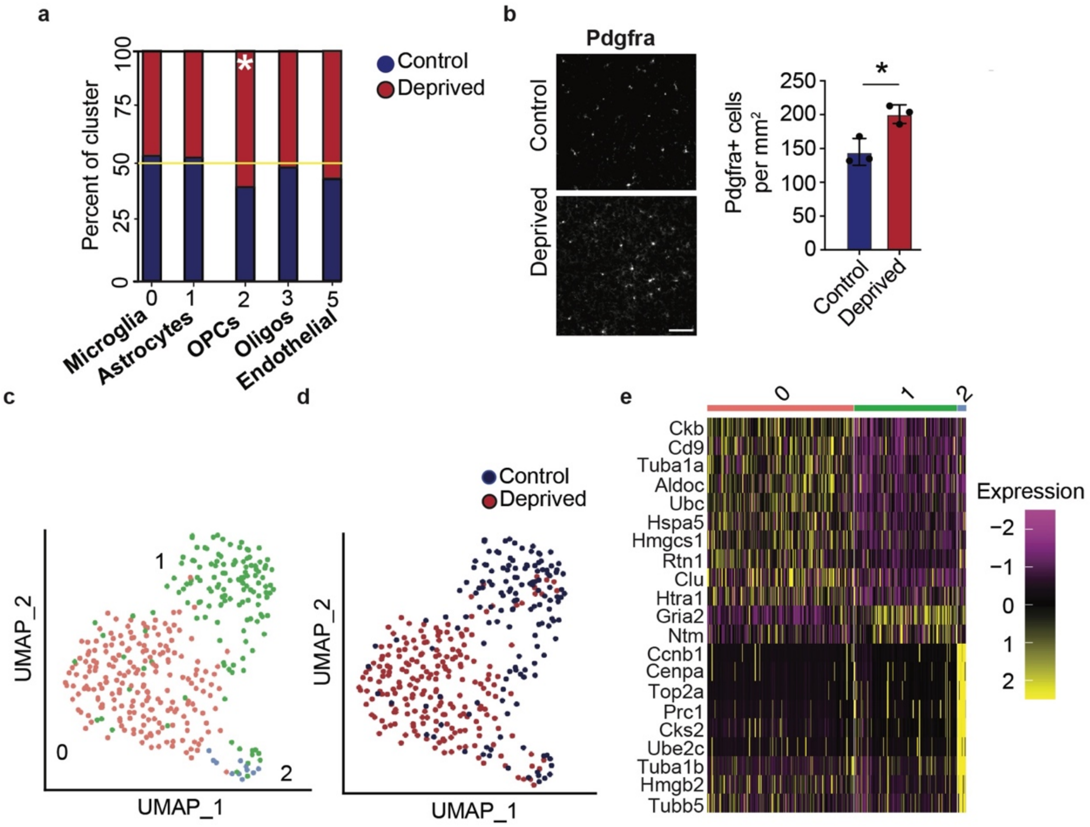

a) Data from Fig. 1F-H shown as a bar plot of relative proportions of control and deprived cells collapsed by cell type. (Chi-square test, *p<0.01).

b) Representative images and quantification of PDGFRα+ oligodendrocyte progenitor cells in L4 of the barrel cortex. (n=3 mice, paired t-test).

c-d) UMAP plot showing astrocyte-only reclustering colored by cluster (C), and condition (D) (n=357 cells, resolution = 0.6).

e) Heatmap of top nine genes enriched in each astrocyte cluster ordered by natural log fold change. *Htra1*, in the top 25 genes, is also included. (MAST DE test, $P_{Adj.} < 0.001$).

*Statistics: All tests shown are two-tailed. *p<0.05, **p<0.01, ***p<0.001, ****p<0.0001 unless otherwise noted. Graphs shown as mean ± SD (bar graphs) or mean ± SEM (stacked bar graphs).*

Supplemental Figure 4: Quality control and additional analyses of microglial single cell sequencing data in Figures 2-4.

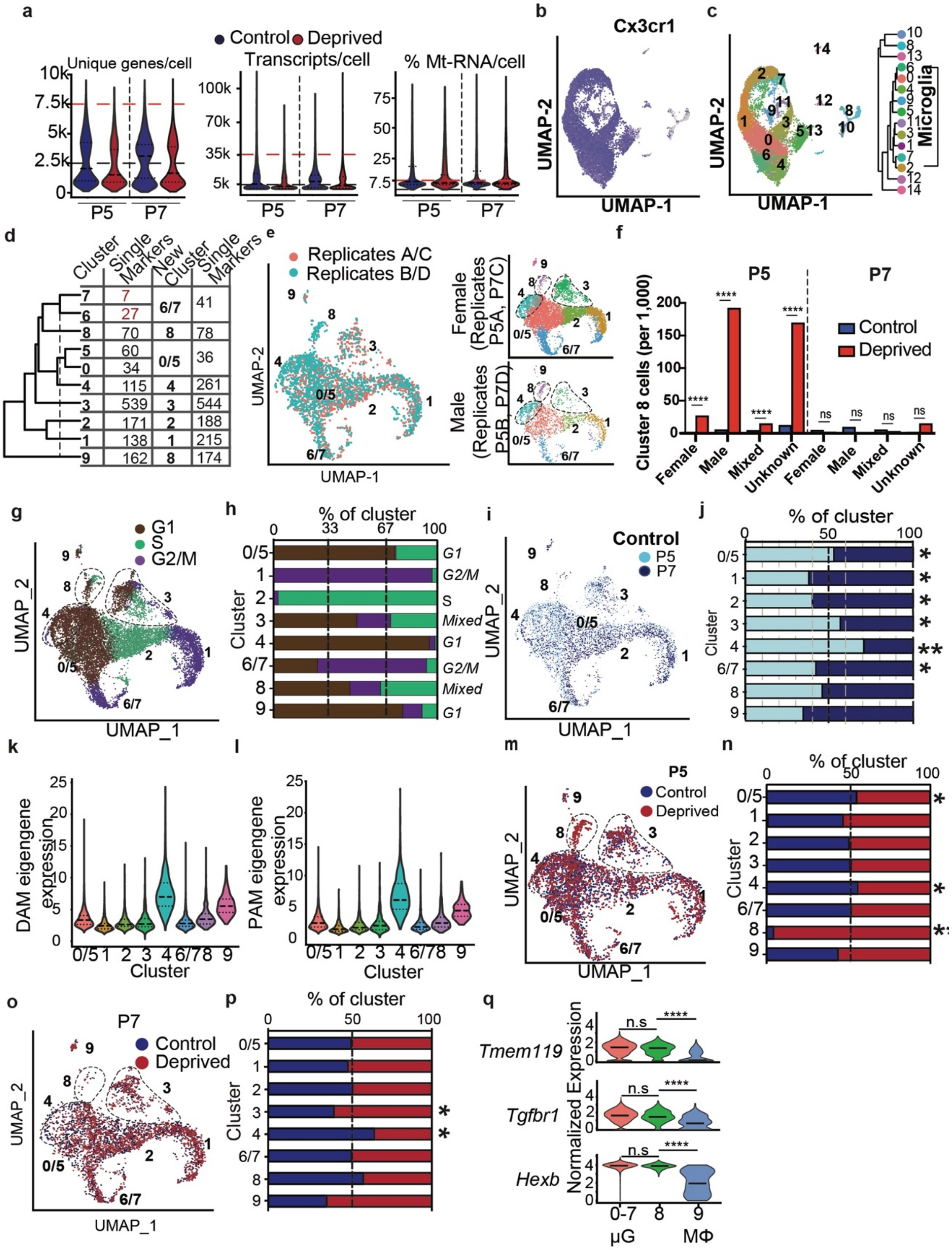

a) Quality control metrics for microglial single cell sequencing (% Mt-RNA/cell: mitochondrial RNA content). Dotted lines indicate minimum and maximum threshold settings. Dashed lines represent median, 1st and 3rd quartiles.

b-c) Feature plot of *Cx3cr1* and unsupervised clustering of all thresholded cells used to select myeloid cells (*Cx3cr1*+) for subsequent analysis.

d) Table showing the number of uniquely upregulated genes (lfc >0.15, p.adj $< 10^{-5}$) before and after combining clusters 6/7 and 0/5. The dotted line shows the threshold below which clusters were combined due to few unique DEGs in both lower branches. The resultant clusters were not closely related to any other clusters with few unique DEGs.

e) Comparison of biological replicates bioinformatically segregated via expression of male-specific genes *Ddx3y* and *Eif2s3y* and female-specific genes *Xist* and *Tsix*, normalized for abundance. Female and Male replicates also shown colored by cluster in UMAP space. (Replicate A: 3 female mice at P5; Replicate B: 3 male mice at P5; Replicate C: 3 female mice at P7; Replicate D: 1 male mouse at P7)

f) Cluster 8 enrichment in definitively female (*Xist/Tsix*+; *Ddx3y/Eif2s3y*-), definitively male (*Ddx3y/Eif2s3y*+; *Xist/Tsix*-), mixed (*Xist/Tsix*+;*Ddx3y/Eif2s3y*-) and unknown(*Xist/Tsix*-;*Ddx3y/Eif2s3y*-) cells.

g) UMAP plot showing cell cycle phase assignment determined using annotation from [134].

h) Quantification of cluster composition by cell cycle phase. X-axis=% cells per cluster in G1, S, or G2/M. Labels to the right indicate that cluster's predominant phase.

i-j) Age comparison by feature plot (i) and quantification (j) , showing only control cells, normalized for abundance. (Chi-square test with Bonferroni correction, *adj. $p<0.01$, **adj. $p < 10^{-25}$).

k) DAM Eigengene signature expression by cluster. The eigengene represents the 83 genes upregulated by DAMS that were also found in this dataset (lfc > 1.5, adj. $p < 10^{-8}$) [58]. Dotted lines represent median and 1st and 3rd quartiles.

l) PAM Eigengene signature expression by cluster. The eigengene represents the 42 genes conserved between two published datasets of a developmental PAM signature that were also expressed in this dataset. (lfc > 1.5, adj. $p < 10^{-8}$) [9,10]. Dotted lines represent median and 1st and 3rd quartiles.

m-p) UMAP feature plots and quantification of percent composition of each cluster at P5 (**m-n**) and P7 (**o-p**). (Chi-Square test with Bonferroni correction, *adj. $p<0.01$, **adj. $p < 10^{-25}$).

q) Canonical microglial genes across microglial clusters 0-6 (pooled), microglial cluster 8, and putative macrophage cluster 9. Line = median. (MAST DE test, ****$p<10^{-25}$).

*Statistics: All tests shown are two-tailed. *p<0.05, **p<0.01, ***p<0.001, ****p<0.0001 unless otherwise noted. Graphs shown as mean ± SD (bar graphs) or mean ± SEM (stacked bar graphs).*

Supplemental Figure 5: Validation and additional analyses of IFITM3 expression after whisker deprivation.

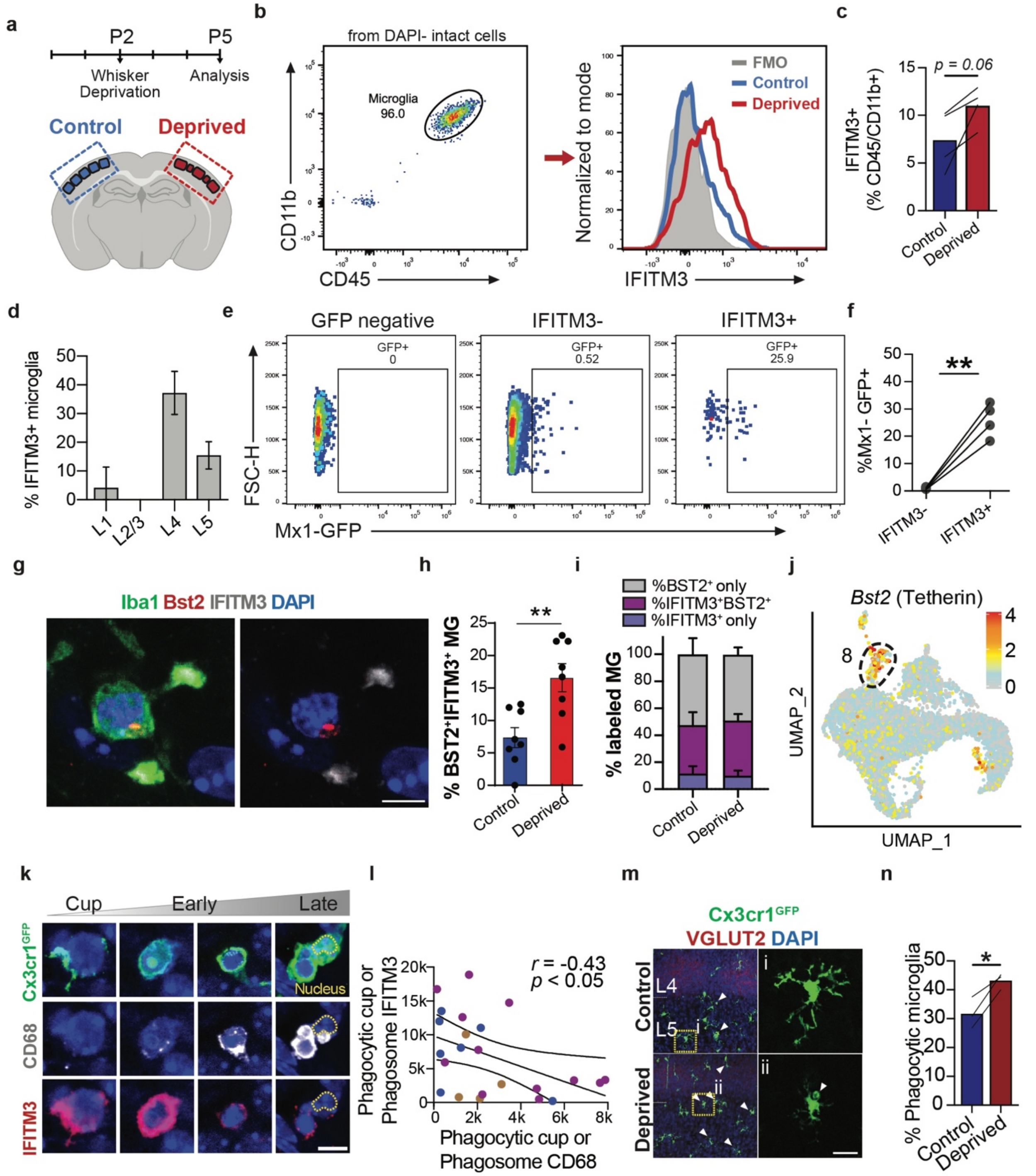

a) Schematic and experimental design for IFITM3 *in situ* validation experiments.

b-c) Representative gating strategy, histogram, and quantification of IFITM3 surface protein expression in Cd11b^{+}/CD45^{low} microglia in control and deprived hemispheres (FMO: fluorescence minus one negative control). Lines represent control and deprived hemispheres from individual mice. (n = 4 mice,paired t-test).

d) Percent IFITM3+ microglia stratified by cortical layers in deprived cortex, see **Fig. 3d** for representative images (n = 3 mice).

f) Representative flow cytometric gating strategy of Mx1-GFP+ microglia from IFITM3$^-$ vs. IFITM3$^+$ populations. Lines connect values from the same mouse (n = 4 mice, paired t-test).
g) Image showing colocalization of BST2/Tetherin (Red) with Iba1 (green, microglia, outlined with white dotted line); IFITM3 (white); and in the deprived barrel cortex. (Scale bar = 10 µm).
h) Quantification of double-positive Bst2+/Ifitm3+ microglia as a percentage of total microglia. (n = 2-3 images per condition from 3 mice, Welch's t-test).
i) Percent of Iba1+ microglia expressing IFITM3 only (blue), Bst2(Tetherin) only (grey) or both (purple). (n=3 mice).
j) Normalized expression of *Bst2* in microglia sequenced in Fig. 2.
k) Representative images showing changes in IFITM3 and CD68 expression at different stages of phagocytosis (Yellow dotted line = microglial nucleus, Scale bar = 5 µm)
l) Correlation of CD68 and IFITM3 mean fluorescence intensity per phagocytic compartment, including both phagocytic cups and phagosomes/phagolysosomes (n = 23 cells from 3 mice, r = Spearman correlation coefficient).
m) Representative images of microglia in control and deprived cortex, inset: single microglia (scale = 50 µm, arrowheads= phagosomes/phagocytic cups).
n) Percent microglia containing at least one phagosome or phagocytic cup in control vs. deprived cortices (P5, n = 3, paired t-test).
*Statistics: All tests shown are two-tailed. *p<0.05, **p<0.01, ***p<0.001, ****p<0.0001 unless otherwise noted. Graphs shown as mean ± SD (bar graphs) or mean ± SEM (stacked bar graphs).*

Supplemental Figure 6: Additional analysis of putative neuron-digesting cluster 3

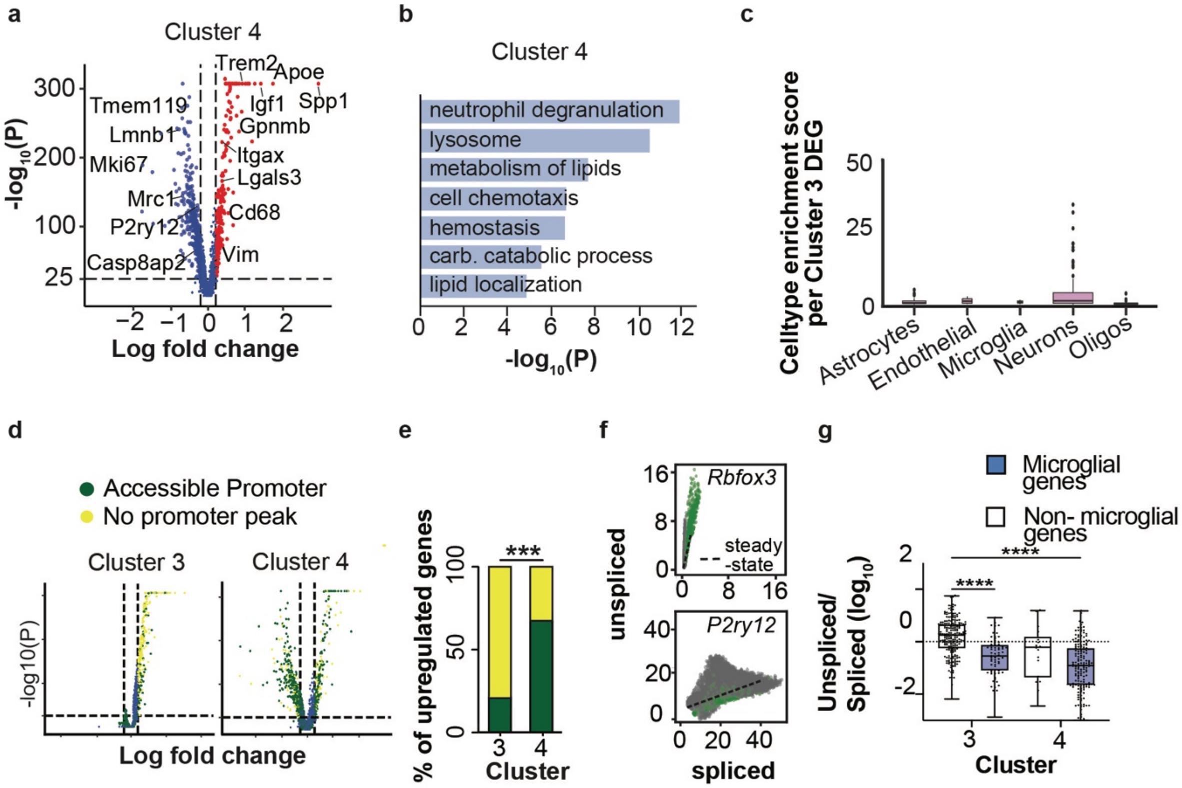

a-b) Volcano plot and gene ontology analysis of DEGs in cluster 4, which is analyzed in subsequent panels in comparison to cluster 3.

c) Rank plot of genes enriched in cluster 3 (natural log fold change > 0.25, adj. $p < 10^{-10}$) that are canonical for specified cell type expressed as fold- enrichment relative to next ranked cell type. Canonical gene expression values derived from a published bulk-sequencing dataset[122].

d) Volcano plots in Fig. 4**c** (cluster 3) and S6**b** (cluster 4) colored by genes with accessible promoters (green) vs. no promoter peak (gray) from ATAC-seq data from P30 somatosensory cortex microglia.[70] "Accessible promoter" defined as ATAC-seq reads > 10th percentile of all peaks, "no promoter peak" defined as reads below 10% threshold.

e) Bar plot of differentially expressed genes with accessible promoters vs. no promoter peak in clusters 3 and 4 (Chi-Square test).

f) Representative plots of transcript status for a canonical neuronal gene (*Rbfox3,* which encodes NeuN*)* vs. a microglial gene (*P2ry12*). Each dot represents one cell; units are in transcript counts per cell. Green dots are cells in cluster 3; grey dots are cells in all other clusters.

g) Ratio of unspliced:spliced transcripts ($\log_{10}$) for enriched genes in clusters 3 and 4, for canonical microglial genes (blue) vs. genes enriched in other cell types (white). "Enriched" = 10x higher FPKM in microglia than the mean of other cell types from [122]. Box and whisker plots show data range, median, and first to third quartiles. (Welch's ANOVA with Tamhane's T2 test for multiple comparisons).

*Statistics: All tests shown are two-tailed. *p<0.05, **p<0.01, ***p<0.001, ****p<0.0001 unless otherwise noted. Graphs shown as mean ± SD (bar graphs) or mean ± SEM (stacked bar graphs).*

Supplemental Figure 7: Characterization of dysmorphic microglia in the *Ifnar1-/-* mouse.

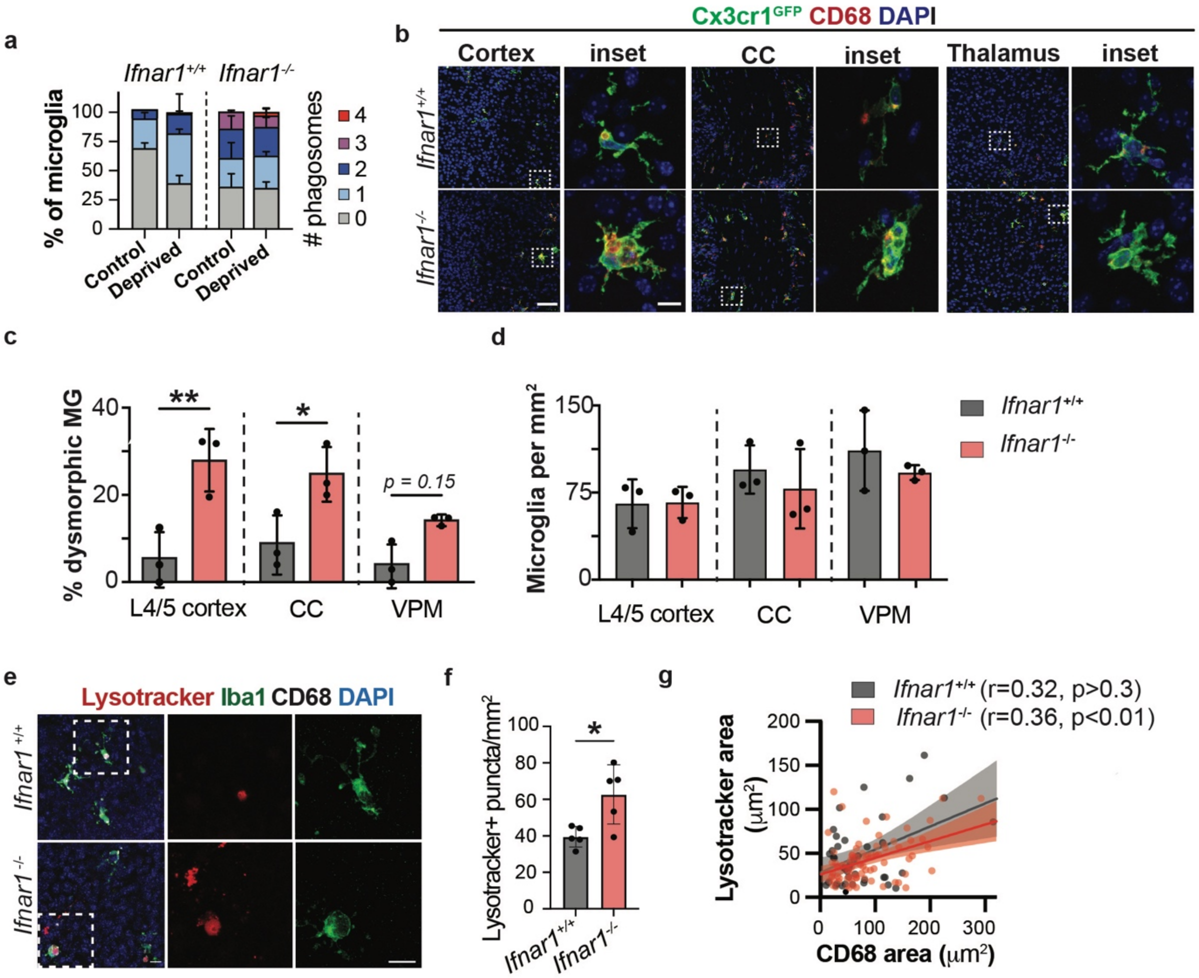

a) Data from Fig. 5F plotted to highlight number of phagocytic compartments per microglia. (n = 3 mice per genotype).
b) Representative images showing microglial morphology in different brain regions. (Scale bar = 50 µm (left, low power), 10 µm (inset, high power)).
c) Dysmorphic ("bubble") microglia as a percent of total microglia per brain region. (n=3 mice per genotype, 2-way ANOVA with Sidak's post-hoc test).
d) Microglial density in *Ifnar1*$^{+/+}$ and *Ifnar1*$^{-/-}$ mice by brain region. (n=3 mice per genotype, 2-way ANOVA with Sidak's post-hoc test).
e) Representative images of LysoTracker Red labeled lysosomes within microglia in *Ifnar1*$^{+/+}$ and *Ifnar1*$^{-/-}$ mice. (Scale bar = 10 µm)
f) Lysotracker+ puncta within microglia in *Ifnar1*$^{+/+}$ and *Ifnar1*$^{-/-}$ mice (n = 5 mice per genotype, Welch's t-test).
g) Correlation between CD68 area and Lysotracker area per cell in cells with detectable signal in both channels. (n=5 mice per genotype, r = Spearman correlation coefficient).
*Statistics: All tests shown are two-tailed. *p<0.05, **p<0.01, ***p<0.001, ****p<0.0001 unless otherwise noted. Graphs shown as mean ± SD (bar graphs) or mean ± SEM (stacked bar graphs).*

Supplemental Figure 8: Additional analysis of microglial contact with markers of neuronal cell stress and apoptosis

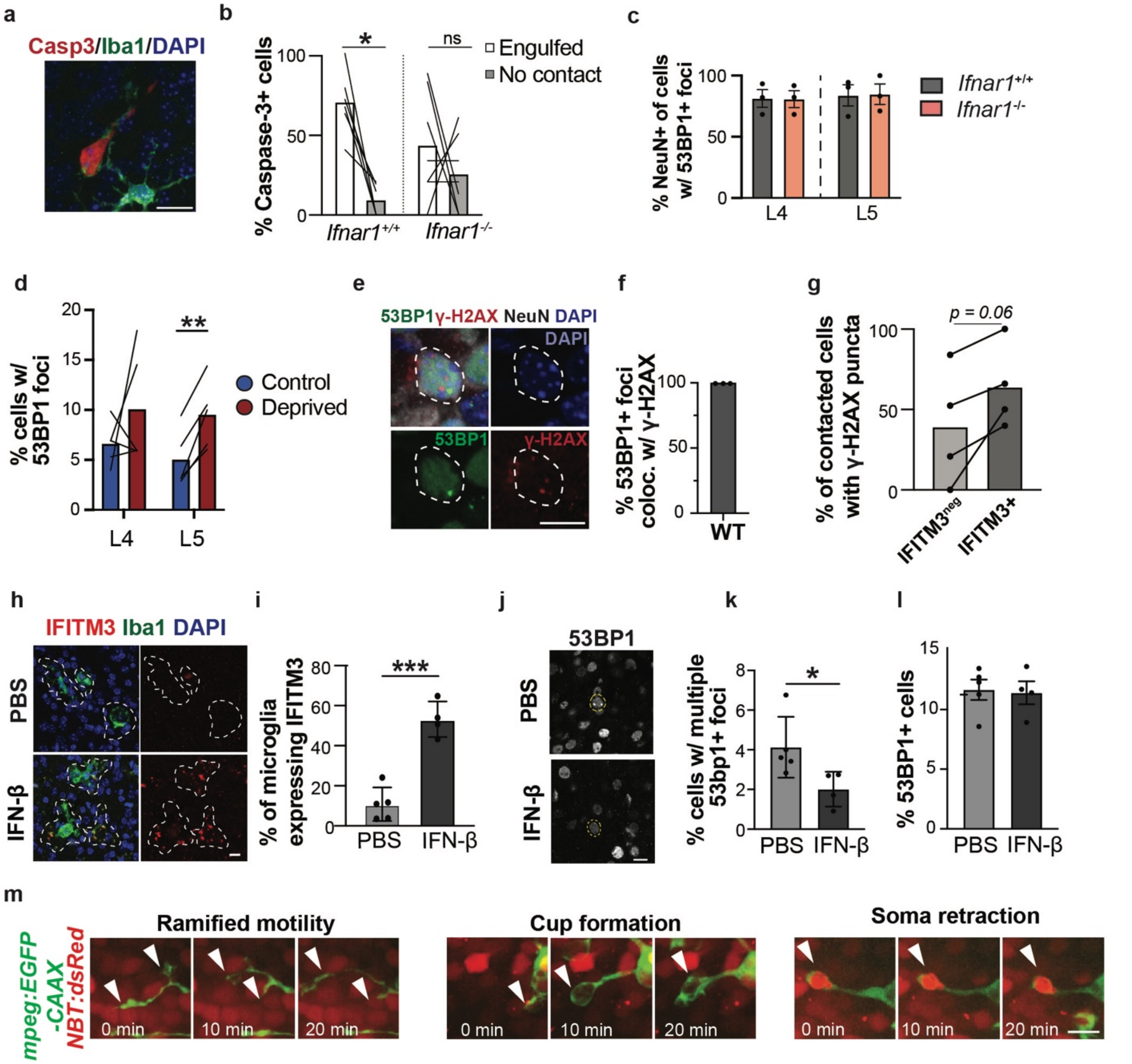

a) Representative micrograph of a microglia (green, Iba1) contacting a Caspase-3+ neuron (red). Scale= 10 µm.
b) Quantification of mircroglial contact with cleaved caspase-3+ cells in *Ifnar1*$^{+/+}$ and *Ifnar1*$^{-/-}$ mice. White bars: % of caspase+ cells completely engulfed by a microglia. Grey: % of caspase-3+ cells with no microglial contact. The remaining cells were in partial contact but not engulfed as shown in g. (n = 6 *Ifnar1*$^{+/+}$ mice, 7 *Ifnar1*$^{-/-}$ mice, 2-way RM ANOVA with Sidak's post-hoc test).
c) Percent of 53BP1+ foci-containing cells that also express the neuronal marker NeuN (n = 3 mice per genotype).
d) Percent cells with 53BP1+ foci in control vs. whisker deprived barrel cortex in layer 4 (L4) or layer 5 (L5), lines connect control and deprived cortices from individual mice (n=5 mice, 2-way RM ANOVA with Sidak's post-hoc test).
e) Representative images showing colocalization of γ-H2AX and 53BP1 foci within a neuronal nucleus. (Scale bar = 5 µm)
f) Quantification of percent 53BP1 foci+ cells that also had γ-H2AX+ foci. (n=3 mice, paired t-test).
g) Quantification of the percent of cells in contact with microglia lacking IFITM3 protein expression (IFITM3^{neg}) or expressing IFITM3 (IFITM3^{+}) that have at least one γ-H2AX puncta. (n=3 mice, paired t-test).

h) Representative image of IFITM3 expression in microglia 24 hours after IFN-β or PBS i.c.v. injection at P4. Dotted lines outline individual microglia (Scale bar = 10 μm).
i) Quantification of percent of microglia expressing IFITM3 protein following PBS or IFN-β i.c.v. injection. (n = 5 mice with PBS, 4 mice with IFN- β, t-test).
j) Representative image of 53BP1+ foci in L2/3 cortex 24 hours after PBS or IFN-β-injection (scale = 10 μm).
k) Quantification of cells containing multiple (>2) 53BP1+ foci 24 hours after PBS or IFN-β injection (n = 5 mice with PBS, 4 mice with IFN- β, t-test).
l) Quantification showing percent of cells containing 53bp1 foci following PBS or IFN-β injection. (n = 5 mice with PBS, 4 mice with IFN- β).
m) Representative images defining the labels used in Fig. 6m. White arrowheads show interactions between the microglial process (*mpeg:EGFP-CAAX*) and surrounding neuronal cell bodies (*NBT:dsRed*). (Scale bar = 10 μm).

*Statistics: All tests shown are two-tailed. *p<0.05, **p<0.01, ***p<0.001, ****p<0.0001 unless otherwise noted. Graphs shown as mean ± SD (bar graphs) or mean ± SEM (stacked bar graphs).*

Supplemental Figure 9: Comparison of single-cell microglial sequencing in various disease and aging models with IFN-I responsive cluster 8.

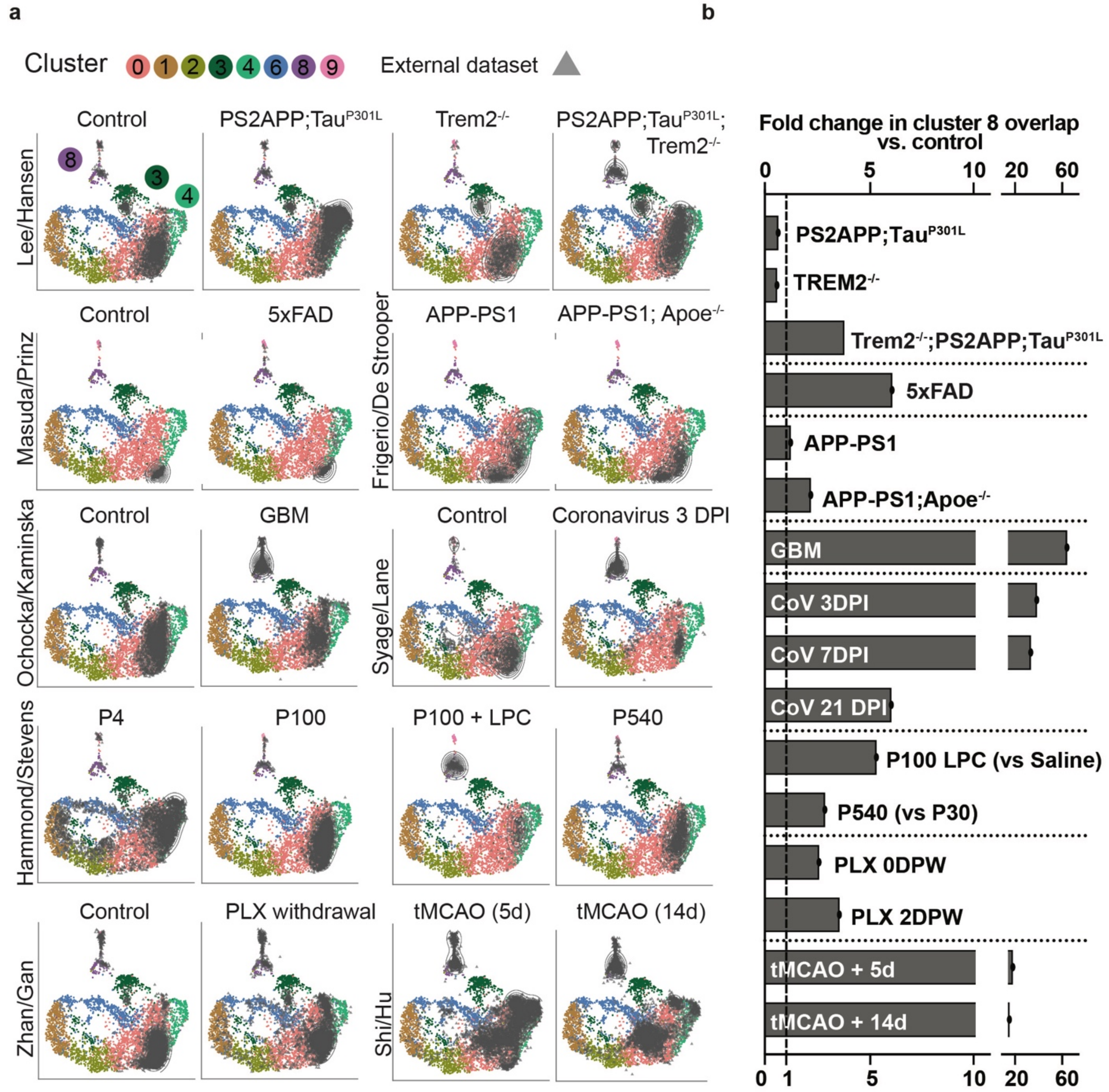

a) Comparison of various microglial single-cell sequencing datasets from different disease states and ages with the single-cell dataset analyzed in this paper. The microglial P5/P7 dataset (colored dots) was reclustered to create a reference PCA and UMAP map which other datasets (grey triangles) were aligned to. Published datasets shown are described and referenced in Supplementary Table 9[9,86–92].

b) Bar plot showing enrichment of cluster 8-like cells in the datasets shown in a) relative to the controls used in each study.

Supplemental Figure 10: Characterization of neurotropic SARS-CoV-2 infection.

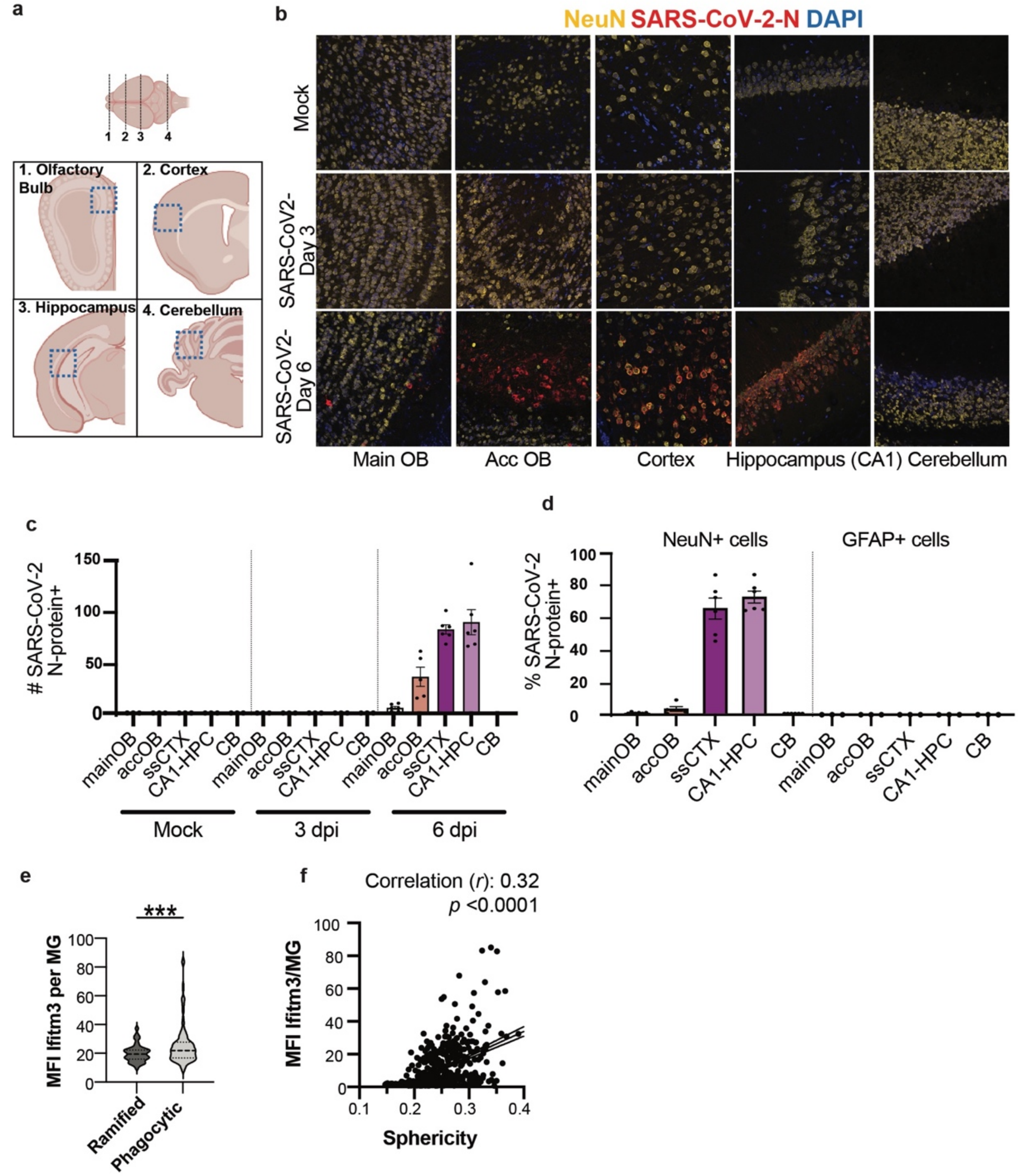

a-b) Schematic and representative images of brain regions after mock infection, and 3 or 6 days post SARS-CoV-2 infection, labeled for SARS-CoV-2 N-protein and NeuN (neurons). Main OB: Olfactory Bulb, Acc OB: Accessory Olfactory Bulb, Cortex: somatosensory.

c) Number of SARS-CoV-2 N-protein+ cells in the indicated brain regions in mock infected, 3 dpi, and 6 dpi mice. (n=2 mice per condition).

d) Neurons (NeuN+), astrocytes (GFAP+) or microglia (Iba1+) positive for SARS-CoV-2 N-protein at 6 dpi. (3 images per region from each of n=2 mice).

e) Quantification of IFITM3 intensity in phagocytic and non-phagocytic (ramified) cells from SARS-CoV-2 infected brains at 6 dpi (n = 2 mice, Welch's t-test).

f) Correlation of microglial sphericity and IFITM3 intensity in Iba1+ cells from mock and infected brains. (n = 2 mock, 3 mice at 3 DPI, 3 mice at 6 DPI, r = Spearman correlation coefficient).

*Statistics: All tests shown are two-tailed. *p<0.05, **p<0.01, ***p<0.001, ****p<0.0001 unless otherwise noted. Graphs shown as mean ± SD (bar graphs) or mean ± SEM (stacked bar graphs).*

Acknowledgements:

We are grateful to members of the Molofsky Lab for helpful comments on the manuscript, Dr. Rafael Han for assistance with tissue preparation, and Dr. Ari Molofsky for helpful feedback on the manuscript. Thanks to the Chan-Zuckerberg Biohub for sequencing support. **Funding*:*** A.V.M is supported by the Pew Charitable Trusts, NIMH (R01MH119349 and DP2MH116507), and the Burroughs Welcome Fund. T.J.N. was supported by NIMH RF1MH121268. L.C.D. received support from the Matilda Edlund Scholarship and the Genentech Fellowship. P.T.N. is supported by a graduate research fellowship from the National Science Foundation (Grant #1650113). C.E. was supported by a gift from Marilyn Waldman. C.C. was supported by NIA RF1AG061874.

Author contributions:

Conceptualization: A.V.M and L.C.D.; Methodology, L.C.D., A.V.M, P.T.N., I.D.V., C.C.E., H. N-I., Y.X., B.R., C.C., R.A. B.S., H.N., N.J.S.; Investigation: L.C.D., P.T.N., I.D.V, S.E.T., C.C.E, E.W., B.R., Y.X., P.V.L., C.L.L., B.C., H.N., N.J.S.; Writing – Original Draft, L.C.D., P.T.N., C.C.E., and A.V.M.; Writing – Review & Editing, all co-authors; Funding Acquisition, A.V.M. Resources, A.V.M., C.C., R.A., Supervision, A.V.M., T.N., C.C., R.A., B.S., and I.D.V.

Declaration of interests: The authors declare no competing interests.

Data availability: Supplement contains additional data. All data needed to evaluate the conclusions in the paper are present in the paper or the Supplementary Materials. Searchable database available at https://www.annamolofskylab.org/microglia-sequencing. RNA sequencing data is available through GEO at GSE173173. Any additional data needed to evaluate the paper will be provided upon request.

Code availability: R and Python code used to analyze single cell datasets is available on GitHub at https://github.com/lcdorman/IFNresponseCode.

Bibliography

1. Arguello, P. A. & Gogos, J. A. Genetic and cognitive windows into circuit mechanisms of psychiatric disease. *Trends in Neurosciences* **35**, 3–13 (2012).
2. Forrest, M. P., Parnell, E. & Penzes, P. Dendritic structural plasticity and neuropsychiatric disease. *Nature Reviews Neuroscience* **19**, 215–234 (2018).
3. Bitzenhofer, S. H., Pöpplau, J. A., Chini, M., Marquardt, A. & Hanganu-Opatz, I. L. A transient developmental increase in prefrontal activity alters network maturation and causes cognitive dysfunction in adult mice. *Neuron* (2021). doi:10.1016/j.neuron.2021.02.011
4. Medendorp, W. E. *et al.* Selective postnatal excitation of neocortical pyramidal neurons results in distinctive behavioral and circuit deficits in adulthood. *iScience* **24**, (2021).
5. Vainchtein, I. D. & Molofsky, A. V. Astrocytes and Microglia: In Sickness and in Health. *Trends in Neurosciences* (2020). doi:10.1016/j.tins.2020.01.003
6. Allen, N. J. & Lyons, D. A. Glia as architects of central nervous system formation and function. *Science* (2018). doi:10.1126/science.aat0473
7. Prinz, M., Jung, S. & Priller, J. Microglia Biology: One Century of Evolving Concepts. *Cell* (2019). doi:10.1016/j.cell.2019.08.053
8. Frost, J. L. & Schafer, D. P. Microglia: Architects of the Developing Nervous System. *Trends in Cell Biology* **26**, 587–597 (2016).
9. Hammond, T. R. *et al.* Single-Cell RNA Sequencing of Microglia throughout the Mouse Lifespan and in the Injured Brain Reveals Complex Cell-State Changes. *Immunity* (2019). doi:10.1016/j.immuni.2018.11.004
10. Li, Q. *et al.* Developmental Heterogeneity of Microglia and Brain Myeloid Cells Revealed by Deep Single-Cell RNA Sequencing. *Neuron* (2019). doi:10.1016/j.neuron.2018.12.006
11. Gosselin, D. *et al.* An environment-dependent transcriptional network specifies human microglia identity. *Science (80-.).* (2017). doi:10.1126/science.aal3222
12. Gosselin, D. *et al.* Environment drives selection and function of enhancers controlling tissue-specific macrophage identities. *Cell* (2014). doi:10.1016/j.cell.2014.11.023
13. Badimon, A. *et al.* Negative feedback control of neuronal activity by microglia. *Nature* (2020). doi:10.1038/s41586-020-2777-8
14. Lavin, Y. *et al.* Tissue-resident macrophage enhancer landscapes are shaped by the local microenvironment. *Cell* **159**, 1312–1326 (2014).
15. Chovatiya, R. & Medzhitov, R. Stress, inflammation, and defense of homeostasis. *Molecular Cell* **54**, 281–288 (2014).
16. Van Der Loos, H. & Woolsey, T. A. Somatosensory cortex: Structural alterations following early injury to sense organs. *Science (80-.).* (1973). doi:10.1126/science.179.4071.395
17. Sehara, K. *et al.* Whisker-Related Axonal Patterns and Plasticity of Layer 2/3 Neurons in

the Mouse Barrel Cortex. *J. Neurosci.* (2010). doi:10.1523/jneurosci.6096-09.2010

18. Erzurumlu, R. S. & Gaspar, P. Development and critical period plasticity of the barrel cortex. *Eur. J. Neurosci.* (2012). doi:10.1111/j.1460-9568.2012.08075.x
19. Sehara, K. & Kawasaki, H. Neuronal circuits with whisker-related patterns. *Mol. Neurobiol.* (2011). doi:10.1007/s12035-011-8170-8
20. Sugimoto, T. *et al.* Apoptotic cascade of neurons in the subcortical sensory relay nuclei following the neonatal infraorbital nerve transection. *Brain Res.* (1999). doi:10.1016/S0006-8993(99)01237-8
21. Baldi, A. *et al.* Deafferentation-induced apoptosis of neurons in thalamic somatosensory nuclei of the newborn rat: Critical period and rescue from cell death by peripherally applied neurotrophins. *Eur. J. Neurosci.* (2000). doi:10.1046/j.1460-9568.2000.00119.x
22. Woolsey, T. A. & Wann, J. R. Areal changes in mouse cortical barrels following vibrissal damage at different postnatal ages. *J. Comp. Neurol.* (1976). doi:10.1002/cne.901700105
23. Jeanmonod, D., Rice, F. L. & Van der Loos, H. Mouse somatosensory cortex: Alterations in the barrelfield following receptor injury at different early postnatal ages. *Neuroscience* (1981). doi:10.1016/0306-4522(81)90222-0
24. Stogsdill, J. A. *et al.* Astrocytic neuroligins control astrocyte morphogenesis and synaptogenesis. *Nature* **551**, 192–197 (2017).
25. Hoshiko, M., Arnoux, I., Avignone, E., Yamamoto, N. & Audinat, E. Deficiency of the Microglial Receptor CX3CR1 Impairs Postnatal Functional Development of Thalamocortical Synapses in the Barrel Cortex. *J. Neurosci.* (2012). doi:10.1523/jneurosci.1167-12.2012
26. Gunner, G. *et al.* Sensory lesioning induces microglial synapse elimination via ADAM10 and fractalkine signaling. *Nat. Neurosci.* (2019). doi:10.1038/s41593-019-0419-y
27. Rebsam, A., Seif, I. & Gaspar, P. Refinement of thalamocortical arbors and emergence of barrel domains in the primary somatosensory cortex: A study of normal and monoamine oxidase A knock-out mice. *J. Neurosci.* **22**, 8541–8552 (2002).
28. Rice, F. L., Gomez, C., Barstow, C., Burnet, A. & Sands, P. AComparative analysis of the development of the primary somatosensory cortex: Interspecies similarities during barrel and laminar development. *J. Comp. Neurol.* **236**, 477–495 (1985).
29. Gunner, G. *et al.* Sensory lesioning induces microglial synapse elimination via ADAM10 and fractalkine signaling. *Nat. Neurosci.* **22**, 1075–1088 (2019).
30. Adam, M., Potter, A. S. & Potter, S. S. Psychrophilic proteases dramatically reduce single-cell RNA-seq artifacts: A molecular atlas of kidney development. *Dev.* (2017). doi:10.1242/dev.151142
31. Mangin, J. M., Li, P., Scafidi, J. & Gallo, V. Experience-dependent regulation of NG2 progenitors in the developing barrel cortex. *Nat. Neurosci.* (2012). doi:10.1038/nn.3190
32. Singh, S. K. *et al.* Astrocytes Assemble Thalamocortical Synapses by Bridging NRX1α and NL1 via Hevin. *Cell* (2016). doi:10.1016/j.cell.2015.11.034
33. Ferris, H. A. *et al.* Loss of astrocyte cholesterol synthesis disrupts neuronal function and

alters whole-body metabolism. *Proc. Natl. Acad. Sci. U. S. A.* (2017). doi:10.1073/pnas.1620506114

34. Valenza, M. *et al.* Disruption of astrocyte-neuron cholesterol cross talk affects neuronal function in Huntington's disease. *Cell Death Differ.* (2015). doi:10.1038/cdd.2014.162
35. Pfrieger, F. W. Role of cholesterol in synapse formation and function. *Biochimica et Biophysica Acta - Biomembranes* (2003). doi:10.1016/S0005-2736(03)00024-5
36. Mauch, D. H. *et al.* CNS synaptogenesis promoted by glia-derived cholesterol. *Science (80-.).* (2001). doi:10.1126/science.294.5545.1354
37. Tsai, H. I., Tsai, L. H., Chen, M. Y. & Chou, Y. C. Cholesterol deficiency perturbs actin signaling and glutamate homeostasis in hippocampal astrocytes. *Brain Res.* (2006). doi:10.1016/j.brainres.2006.05.081
38. Cybulska-Klosowicz, A., Zakrzewska, R., Pyza, E., Kossut, M. & Schachner, M. Reduced plasticity of cortical whisker representation in adult tenascin-C-deficient mice after vibrissectomy. *Eur. J. Neurosci.* (2004). doi:10.1111/j.1460-9568.2004.03605.x
39. McRae, P. A., Rocco, M. M., Kelly, G., Brumberg, J. C. & Matthews, R. T. Sensory Deprivation Alters Aggrecan and Perineuronal Net Expression in the Mouse Barrel Cortex. *J. Neurosci.* (2007). doi:10.1523/jneurosci.5425-06.2007
40. Grau, S. *et al.* The role of human HtrA1 in arthritic disease. *J. Biol. Chem.* (2006). doi:10.1074/jbc.M500361200
41. Murwantoko *et al.* Binding of proteins to the PDZ domain proteolytic activity of HtrA1 serine protease. *Biochem. J.* (2004). doi:10.1042/BJ20040435
42. Tsuchiya, A. *et al.* Expression of mouse HtrA1 serine protease in normal bone and cartilage and its upregulation in joint cartilage damaged by experimental arthritis. *Bone* (2005). doi:10.1016/j.bone.2005.03.015
43. Lin, M. K. *et al.* HTRA1, an age-related macular degeneration protease, processes extracellular matrix proteins EFEMP1 and TSP1. *Aging Cell* (2018). doi:10.1111/acel.12710
44. Hong, S. *et al.* Complement and microglia mediate early synapse loss in Alzheimer mouse models. *Science (80-.).* (2016). doi:10.1126/science.aad8373
45. Schafer, D. P. *et al.* Microglia sculpt postnatal neural circuits in an activity and complement-dependent manner. *Neuron* (2012). doi:10.1016/j.neuron.2012.03.026
46. Miyamoto, A. *et al.* Microglia contact induces synapse formation in developing somatosensory cortex. *Nat. Commun.* (2016). doi:10.1038/ncomms12540
47. Nguyen, P. T. *et al.* Microglial Remodeling of the Extracellular Matrix Promotes Synapse Plasticity. *Cell* (2020). doi:10.1016/j.cell.2020.05.050
48. Boada-romero, E. *et al.* Mechanisms and physiology of the clearance of dead cells by efferocytosis. *Nat. Rev. Cell Biol.* (2020).
49. Fourgeaud, L. *et al.* TAM receptors regulate multiple features of microglial physiology. *Nature* **532**, 240–244 (2016).

50. Krasemann, S. *et al.* The TREM2-APOE Pathway Drives the Transcriptional Phenotype of Dysfunctional Microglia in Neurodegenerative Diseases. *Immunity* **47**, 566-581.e9 (2017).

51. Sierra, A. *et al.* Microglia shape adult hippocampal neurogenesis through apoptosis-coupled phagocytosis. *Cell Stem Cell* **7**, 483–495 (2010).

52. Blanquie, O. *et al.* Electrical activity controls area-specific expression of neuronal apoptosis in the mouse developing cerebral cortex. *Elife* (2017). doi:10.7554/eLife.27696

53. Haimon, Z. *et al.* Re-evaluating microglia expression profiles using RiboTag and cell isolation strategies. *Nat. Immunol.* (2018). doi:10.1038/s41590-018-0110-6

54. Bohlen, C. J., Bennett, F. C. & Bennett, M. L. Isolation and Culture of Microglia. *Curr. Protoc. Immunol.* (2019). doi:10.1002/cpim.70

55. Miltenyi, S., Müller, W., Weichel, W. & Radbruch, A. High gradient magnetic cell separation with MACS. *Cytometry* **11**, 231–238 (1990).

56. Marek, R., Caruso, M., Rostami, A., Grinspan, J. B. & Sarma, J. Das. Magnetic cell sorting: A fast and effective method of concurrent isolation of high purity viable astrocytes and microglia from neonatal mouse brain tissue. *J. Neurosci. Methods* **175**, 108–118 (2008).

57. Chris Bennett, F., Bennett, M. L., Gephart, H., Plowey, E. D. & Correspondence, B. A. B. A Combination of Ontogeny and CNS Environment Establishes Microglial Identity. *Neuron* **98**, 1170-1183.e8 (2018).

58. Keren-Shaul, H. *et al.* A Unique Microglia Type Associated with Restricting Development of Alzheimer's Disease. *Cell* **169**, 1276-1290.e17 (2017).

59. McNab, F., Mayer-Barber, K., Sher, A., Wack, A. & O'Garra, A. Type I interferons in infectious disease. *Nature Reviews Immunology* **15**, 87–103 (2015).

60. Hur, J. Y. *et al.* The innate immunity protein IFITM3 modulates γ-secretase in Alzheimer's disease. *Nature* (2020). doi:10.1038/s41586-020-2681-2

61. Bailey, C. C., Zhong, G., Huang, I. C. & Farzan, M. IFITM-family proteins: The cell's first line of antiviral defense. *Annu. Rev. Virol.* (2014). doi:10.1146/annurev-virology-031413-085537

62. Brass, A. L. *et al.* The IFITM Proteins Mediate Cellular Resistance to Influenza A H1N1 Virus, West Nile Virus, and Dengue Virus. *Cell* (2009). doi:10.1016/j.cell.2009.12.017

63. Lee, J. *et al.* IFITM3 functions as a PIP3 scaffold to amplify PI3K signalling in B cells. *Nature* (2020). doi:10.1038/s41586-020-2884-6

64. Uccellini, M. B. & García-Sastre, A. ISRE-Reporter Mouse Reveals High Basal and Induced Type I IFN Responses in Inflammatory Monocytes. *Cell Rep.* (2018). doi:10.1016/j.celrep.2018.11.030

65. Liberatore, R. A. & Bieniasz, P. D. Tetherin is a key effector of the antiretroviral activity of type I interferon in vitro and in vivo. *Proc. Natl. Acad. Sci. U. S. A.* **108**, 18097–18101 (2011).

66. Chistiakov, D. A., Killingsworth, M. C., Myasoedova, V. A., Orekhov, A. N. &

Bobryshev, Y. V. CD68/macrosialin: Not just a histochemical marker. *Lab. Investig.* (2017). doi:10.1038/labinvest.2016.116

67. Uribe-Querol, E. & Rosales, C. Phagocytosis: Our Current Understanding of a Universal Biological Process. *Frontiers in Immunology* (2020). doi:10.3389/fimmu.2020.01066
68. Lancaster, C. E. *et al.* Phagosome resolution regenerates lysosomes and maintains the degradative capacity in phagocytes. *J. Cell Biol.* **220**, (2021).
69. Bergen, V., Lange, M., Peidli, S., Wolf, F. A. & Theis, F. J. Generalizing RNA velocity to transient cell states through dynamical modeling. *Nat. Biotechnol.* (2020). doi:10.1038/s41587-020-0591-3
70. Han, R. T. *et al.* Interleukin-33 coordinates a microglial phagocytic response and limits corticothalamic excitability and seizure susceptibility. *bioRxiv* 2021.08.05.455250 (2021). doi:10.1101/2021.08.05.455250
71. Harris, J. A. *et al.* Anatomical characterization of Cre driver mice for neural circuit mapping and manipulation. *Front. Neural Circuits* **8**, 76 (2014).
72. Madisen, L. *et al.* A robust and high-throughput Cre reporting and characterization system for the whole mouse brain. *Nat. Neurosci.* (2010). doi:10.1038/nn.2467
73. Villani, A. *et al.* Clearance by Microglia Depends on Packaging of Phagosomes into a Unique Cellular Compartment. *Dev. Cell* (2019). doi:10.1016/j.devcel.2019.02.014
74. Ward, I. M., Minn, K., van Deursen, J. & Chen, J. p53 Binding Protein 53BP1 Is Required for DNA Damage Responses and Tumor Suppression in Mice. *Mol. Cell. Biol.* **23**, 2556–2563 (2003).
75. Schultz, L. B., Chehab, N. H., Malikzay, A. & Halazonetis, T. D. P53 Binding Protein 1 (53bp1) Is an Early Participant in the Cellular Response to DNA Double-Strand Breaks. *J. Cell Biol.* **151**, 1381 (2000).
76. Shanbhag, N. M. *et al.* Early neuronal accumulation of DNA double strand breaks in Alzheimer's disease. *Acta Neuropathol. Commun.* **7**, (2019).
77. Madabhushi, R. *et al.* Activity-Induced DNA Breaks Govern the Expression of Neuronal Early-Response Genes. *Cell* **161**, 1592–1605 (2015).
78. Dickey, J. S. *et al.* Intercellular communication of cellular stress monitored by γ-H2AX induction. *Carcinogenesis* **30**, 1686–1695 (2009).
79. Mah, L. J., El-Osta, A. & Karagiannis, T. C. γH2AX: a sensitive molecular marker of DNA damage and repair. *Leuk. 2010 244* **24**, 679–686 (2010).
80. Brown, G. C. & Neher, J. J. Microglial phagocytosis of live neurons. *Nat. Rev. Neurosci.* **15**, 209–216 (2014).
81. Secombes, C. J. & Zou, J. Evolution of interferons and interferon receptors. *Front. Immunol.* **8**, 209 (2017).
82. Boudinot, P., Langevin, C., Secombes, C. J. & Levraud, J. P. The Peculiar Characteristics of Fish Type I Interferons. *Viruses 2016, Vol. 8, Page 298* **8**, 298 (2016).
83. Silva, N. J., Dorman, L. C., Vainchtein, I. D., Horneck, N. C. & Molofsky, A. V. In situ

and transcriptomic identification of microglia in synapse-rich regions of the developing zebrafish brain. *Nat. Commun. 2021 121* **12**, 1–12 (2021).

84. Peri, F. & Nüsslein-Volhard, C. Live imaging of neuronal degradation by microglia reveals a role for v0-ATPase a1 in phagosomal fusion in vivo. *Cell* **133**, 916–927 (2008).
85. Friedman, B. A. *et al.* Diverse Brain Myeloid Expression Profiles Reveal Distinct Microglial Activation States and Aspects of Alzheimer's Disease Not Evident in Mouse Models. *Cell Rep.* (2018). doi:10.1016/j.celrep.2017.12.066
86. Frigerio, C. S. *et al.* The Major Risk Factors for Alzheimer's Disease: Age, Sex, and Genes Modulate the Microglia Response to Aβ Plaques. *Cell Rep.* **27**, 1293–1306 (2019).
87. Zhan, L. *et al.* A MAC2-positive progenitor-like microglial population is resistant to CSF1R inhibition in adult mouse brain. *Elife* **9**, 1–22 (2020).
88. Ochocka, N. *et al.* Single-cell RNA sequencing reveals functional heterogeneity of glioma-associated brain macrophages. *Nat. Commun.* **12**, (2021).
89. Masuda, T. *et al.* Spatial and temporal heterogeneity of mouse and human microglia at single-cell resolution. *Nature* (2019). doi:10.1038/s41586-019-0924-x
90. Shi, L. *et al.* Treg cell-derived osteopontin promotes microglia-mediated white matter repair after ischemic stroke. *Immunity* **54**, 1527-1542.e8 (2021).
91. Lee, S. H. *et al.* Trem2 restrains the enhancement of tau accumulation and neurodegeneration by β-amyloid pathology. *Neuron* **109**, 1283-1301.e6 (2021).
92. Syage, A. R. *et al.* Single-Cell RNA Sequencing Reveals the Diversity of the Immunological Landscape following Central Nervous System Infection by a Murine Coronavirus. *J. Virol.* **94**, (2020).
93. Zhang, Y. *et al.* Interferon-Induced Transmembrane Protein 3 Genetic Variant rs12252-C Associated with Disease Severity in Coronavirus Disease 2019. *J. Infect. Dis.* (2020). doi:10.1093/infdis/jiaa224
94. Hachim, M. Y. *et al.* Interferon-Induced Transmembrane Protein (IFITM3) Is Upregulated Explicitly in SARS-CoV-2 Infected Lung Epithelial Cells. *Front. Immunol.* (2020). doi:10.3389/fimmu.2020.01372
95. Shi, G. *et al.* Opposing activities of IFITM proteins in SARS-CoV-2 infection. *EMBO J.* (2021). doi:10.15252/embj.2020106501
96. Song, E. *et al.* Neuroinvasion of SARS-CoV-2 in human and mouse brain. *J. Exp. Med.* (2021). doi:10.1084/JEM.20202135
97. Liotta, E. M. *et al.* Frequent neurologic manifestations and encephalopathy-associated morbidity in Covid-19 patients. *Ann. Clin. Transl. Neurol.* (2020). doi:10.1002/acn3.51210
98. Taquet, M., Luciano, S., Geddes, J. R. & Harrison, P. J. Bidirectional associations between COVID-19 and psychiatric disorder: retrospective cohort studies of 62 354 COVID-19 cases in the USA. *The Lancet Psychiatry* **8**, 130–140 (2021).

99. Moreau, G. B. *et al.* Evaluation of K18-hACE2 Mice as a Model of SARS-CoV-2 Infection. *Am. J. Trop. Med. Hyg.* (2020). doi:10.4269/ajtmh.20-0762

100. Winkler, E. S. *et al.* SARS-CoV-2 infection of human ACE2-transgenic mice causes severe lung inflammation and impaired function. *Nat. Immunol.* (2020). doi:10.1038/s41590-020-0778-2

101. Israelow, B. *et al.* Mouse model of SARS-CoV-2 reveals inflammatory role of type i interferon signaling. *J. Exp. Med.* (2020). doi:10.1084/JEM.20201241

102. McCray, P. B. *et al.* Lethal Infection of K18-hACE2 Mice Infected with Severe Acute Respiratory Syndrome Coronavirus. *J. Virol.* (2007). doi:10.1128/jvi.02012-06

103. Carossino, M. *et al.* Fatal neuroinvasion of SARS-CoV-2 in K18-hACE2 mice is partially dependent on hACE2 expression. *bioRxiv* (2021).

104. Kumari, P. *et al.* Neuroinvasion and Encephalitis Following Intranasal Inoculation of SARS-CoV-2 in K18-hACE2 Mice. *Viruses* (2021). doi:10.3390/v13010132

105. Baruch, K. *et al.* Aging-induced type I interferon response at the choroid plexus negatively affects brain function. *Science (80-.).* (2014). doi:10.1126/science.1252945

106. Roy, E. R. *et al.* Type I interferon response drives neuroinflammation and synapse loss in Alzheimer disease. *J. Clin. Invest.* (2020). doi:10.1172/JCI133737

107. Minter, M. R. *et al.* Deletion of the type-1 interferon receptor in APPSWE/PS1ΔE9 mice preserves cognitive function and alters glial phenotype. *Acta Neuropathol. Commun.* **4**, 72 (2016).

108. Orre, M. *et al.* Isolation of glia from Alzheimer’s mice reveals inflammation anddysfunction. *Neurobiol. Aging* **35**, 2746–2760 (2014).

109. Oakley, H. *et al.* Intraneuronal β-amyloid aggregates, neurodegeneration, and neuron loss in transgenic mice with five familial Alzheimer’s disease mutations: Potential factors in amyloid plaque formation. *J. Neurosci.* (2006). doi:10.1523/JNEUROSCI.1202-06.2006

110. Mazaheri, F. *et al.* Distinct roles for BAI1 and TIM-4 in the engulfment of dying neurons by microglia. *Nat. Commun. 2014 51* **5**, 1–11 (2014).

111. Huang, Y. *et al.* Microglia use TAM receptors to detect and engulf amyloid β plaques. *Nat. Immunol.* 1–9 (2021). doi:10.1038/s41590-021-00913-5

112. Márquez-Ropero, M., Benito, E., Plaza-Zabala, A. & Sierra, A. Microglial Corpse Clearance: Lessons From Macrophages. *Front. Immunol.* **11**, 506 (2020).

113. Lemke, G. How macrophages deal with death. *Nature Reviews Immunology* **19**, 539–549 (2019).

114. Hansen, D. V., Hanson, J. E. & Sheng, M. Microglia in Alzheimer’s disease. *Journal of Cell Biology* (2018). doi:10.1083/jcb.201709069

115. Liu, Z., Condello, C., Schain, A., Harb, R. & Grutzendler, J. CX3CR1 in microglia regulates brain amyloid deposition through selective protofibrillar amyloid-β phagocytosis. *J. Neurosci.* (2010). doi:10.1523/JNEUROSCI.4403-10.2010

116. Ivashkiv, L. B. & Donlin, L. T. Regulation of type i interferon responses. *Nature Reviews*

Immunology (2014). doi:10.1038/nri3581

117. Brendecke, S. M. & Prinz, M. How type I interferons shape myeloid cell function in CNS autoimmunity. *J. Leukoc. Biol.* **92**, 479–488 (2012).

118. Kumaran Satyanarayanan, S. *et al.* IFN-β is a macrophage-derived effector cytokine facilitating the resolution of bacterial inflammation. *Nat. Commun.* **10**, 1–16 (2019).

119. Ranjbar, S., Haridas, V., Jasenosky, L. D., Falvo, J. V. & Goldfeld, A. E. A Role for IFITM Proteins in Restriction of Mycobacterium tuberculosis Infection. *Cell Rep.* (2015). doi:10.1016/j.celrep.2015.09.048

120. Marín-Teva, J. L. *et al.* Microglia Promote the Death of Developing Purkinje Cells. *Neuron* **41**, 535–547 (2004).

121. Wakselman, S. *et al.* Developmental neuronal death in hippocampus requires the microglial CD11b integrin and DAP12 immunoreceptor. *J. Neurosci.* **28**, 8138–8143 (2008).

122. Zhang, Y. *et al.* An RNA-sequencing transcriptome and splicing database of glia, neurons, and vascular cells of the cerebral cortex. *J. Neurosci.* (2014). doi:10.1523/JNEUROSCI.1860-14.2014

123. Chen, Q., Sun, L. & Chen, Z. J. Regulation and function of the cGAS-STING pathway of cytosolic DNA sensing. *Nature Immunology* (2016). doi:10.1038/ni.3558

124. Li, X. *et al.* Viral DNA Binding to NLRC3, an Inhibitory Nucleic Acid Sensor, Unleashes STING, a Cyclic Dinucleotide Receptor that Activates Type I Interferon. *Immunity* (2019). doi:10.1016/j.immuni.2019.02.009

125. Takaoka, A. & Yamada, T. Regulation of signaling mediated by nucleic acid sensors for innate interferon-mediated responses during viral infection. *International Immunology* (2019). doi:10.1093/intimm/dxz034

126. Wu, J. & Chen, Z. J. Innate immune sensing and signaling of cytosolic nucleic acids. *Annual Review of Immunology* (2014). doi:10.1146/annurev-immunol-032713-120156

127. Kawai, T. & Akira, S. Innate immune recognition of viral infection. *Nature Immunology* (2006). doi:10.1038/ni1303

128. Imai, M. *et al.* Syrian hamsters as a small animal model for SARS-CoV-2 infection and countermeasure development. *Proc. Natl. Acad. Sci. U. S. A.* **117**, 16587–16595 (2020).

129. Sia, S. F. *et al.* Pathogenesis and transmission of SARS-CoV-2 in golden hamsters. *Nature* **583**, 834–838 (2020).

130. Montagutelli, X. *et al.* The B1.351 and P.1 variants extend SARS-CoV-2 host range to mice. *bioRxiv* 2021.03.18.436013 (2021). doi:10.1101/2021.03.18.436013

131. Deczkowska, A. *et al.* Mef2C restrains microglial inflammatory response and is lost in brain ageing in an IFN-I-dependent manner. *Nat. Commun.* (2017). doi:10.1038/s41467-017-00769-0

132. Moore, Z., Mobilio, F., Walker, F. R., Taylor, J. M. & Crack, P. J. Abrogation of type-I interferon signalling alters the microglial response to Aβ1-42. *Sci. Rep.* **10**, 3153 (2020).

133. Hasel, P., Rose, I. V. L., Sadick, J. S., Kim, R. D. & Liddelow, S. A. Neuroinflammatory astrocyte subtypes in the mouse brain. *Nat. Neurosci. 2021 2410* **24**, 1475–1487 (2021).

134. Kowalczyk, M. S. *et al.* Single-cell RNA-seq reveals changes in cell cycle and differentiation programs upon aging of hematopoietic stem cells. *Genome Res.* (2015). doi:10.1101/gr.192237.115

135. Galatro, T. F., Vainchtein, I. D., Brouwer, N., Boddeke, E. W. G. M. & Eggen, B. J. L. Isolation of microglia and immune infiltrates from mouse and primate central nervous system. in *Methods in Molecular Biology* (2017). doi:10.1007/978-1-4939-6786-5_23

136. Dobin, A. *et al.* STAR: Ultrafast universal RNA-seq aligner. *Bioinformatics* (2013). doi:10.1093/bioinformatics/bts635

137. Butler, A., Hoffman, P., Smibert, P., Papalexi, E. & Satija, R. Integrating single-cell transcriptomic data across different conditions, technologies, and species. *Nat. Biotechnol.* (2018). doi:10.1038/nbt.4096

138. Macosko, E. Z. *et al.* Highly Parallel Genome-wide Expression Profiling of Individual Cells Using Nanoliter Droplets. *Cell* (2015). doi:10.1016/j.cell.2015.05.002

139. Hoffman, G. E. & Schadt, E. E. variancePartition: Interpreting drivers of variation in complex gene expression studies. *BMC Bioinformatics* (2016). doi:10.1186/s12859-016-1323-z

140. Zhou, Y. *et al.* Metascape provides a biologist-oriented resource for the analysis of systems-level datasets. *Nat. Commun.* (2019). doi:10.1038/s41467-019-09234-6

141. La Manno, G. *et al.* RNA velocity of single cells. *Nature* (2018). doi:10.1038/s41586-018-0414-6

142. Jung, S. *et al.* Analysis of Fractalkine Receptor CX3CR1 Function by Targeted Deletion and Green Fluorescent Protein Reporter Gene Insertion. *Mol. Cell. Biol.* (2002). doi:10.1128/mcb.20.11.4106-4114.2000

143. Gong, S. *et al.* A gene expression atlas of the central nervous system based on bacterial artificial chromosomes. *Nature* (2003). doi:10.1038/nature02033

144. Prigge, J. R. *et al.* Type I IFNs Act upon Hematopoietic Progenitors To Protect and Maintain Hematopoiesis during Pneumocystis Lung Infection in Mice. *J. Immunol.* (2015). doi:10.4049/jimmunol.1501553

FULL METHODS

- CONTACT FOR REAGENT AND RESOURCE SHARING

Anna Molofsky, anna.molofsky@ucsf.edu

- EXPERIMENTAL MODELS AND SUBJECT DETAILS

Mice: All mouse strains were maintained in the University of California San Francisco specific pathogen–free animal facility, and all animal protocols were approved by and in accordance with the guidelines established by the Institutional Animal Care and Use Committee and Laboratory Animal Resource Center. Mice were housed in a 12-hour light/dark cycle (7 am-7pm) at 68-79° F and 30-70% humidity. Littermate controls were used for all experiments when feasible, and reporter mice were backcrossed >10 generations on a C57Bl/6 background (Cx3cr1-GFP) or Swiss-Webster (Aldh1l1-eGFP). The following mouse strains used are described in the table below and are as referenced in the text: Cx3cr1-GFP (JAX #00582); Aldh1l1-eGFP (Gensat); Ifnar1$^{-/-}$ (JAX #028288); Mx1-GFP (JAX #033219); Mx1-Cre (JAX #003556); Ai14 (JAX #007908); B6.Cg-Tg(K18-ACE2) 2Prlmn/J (JAX #034860); B6SJLTg (APPSwFlLon, PSEN1*M146L*L286V) 6799Vas/ Mmjax (5xFAD, JAX #34840-Jax); Rorb-Ires2-Cre-D (Jax **023526**); Aldh1l1-tdTomato (MMRRC, RRID:MMRRC_036700-UCD)

Zebrafish: Fish were maintained in recirculating habitats at 28.5 °C and on a 14/10-h light/dark cycle. Embryos were collected after natural spawns and incubated at 28.5 °C. Larvae were imaged at 7 days post fertilization (dpf), a developmental stage at which sex cannot be determined. In this study, we used the double transgenic fish *Tg(mpeg:EGFP-CAAX);Tg(NBT:dsRed)* (zfin ID: ZDB-TGCONSTRCT-191211-1 and ZDB-TGCONSTRCT-081023-2) on a casper background to visualize microglia and neurons. All zebrafish protocols were approved by and in accordance with the ethical guidelines established by the UCSF Institutional Animal Care and Use Committee and Laboratory Animal Resource Center (LARC).

- METHOD DETAILS

Whisker lesions: Whisker ablations were performed under hypothermia-induced anesthesia and followed by topical application of lidocaine for pain management. Postnatal day two pups were anesthetized for 3 minutes in ice. An incision was made in the whisker pad along whisker rows B and D of one side of the face, and silver nitrate was used to cauterize the exposed whisker follicles in that row. After topical 2% lidocaine application the mice were reacclimated on a heating pad for at least 15 minutes before being returned to their home cage.

Immunohistochemistry and Confocal Microscopy: For all analyses of barrel cortex, mice were perfused transcardially with ~10 mL of ice-cold PBS followed by ~10 mL of 4% (weight/volume) paraformaldehyde diluted in PBS. For analyses of SARS-CoV-2 infected brains, animals were not perfused and were postfixed by immersion in 4% PFA for 72 hours prior to cryoprotection and sectioning. All other brains were post-fixed in 4% PFA for a minimum of 4 hours and then transferred to a 30% sucrose solution for a minimum of 24 hours. Tangential sections (flat mounts) of the barrel cortex were obtained by dissecting the cortex from the diencephalon following perfusion and flattening the dissected cortices ventral side down between two cryomolds. The sections were placed in between flat toothpicks laid horizontally in the cryomold, and the second mold was pressed down on top of the toothpicks to maintain uniform thickness. Brains were then flash frozen and sliced on a HM 440E freezing microtome (GMI Instruments) or embedded in OCT following 30% sucrose treatment and frozen at -80°C for a minimum of 1 day and then sectioned on a CryoStar NX70 Cryostat (Thermo Fisher) before being mounted on coverslips. Sections from control and deprived hemispheres of individual mice were mounted on the same slides for all experiments.

See resource table below for details of all antibodies used. Immunohistochemistry was performed as follows: brain sections were incubated in a blocking solution consisting of 5% normal goat serum (Thermo Fisher) and 0.1% Triton (Sigma-Aldrich) diluted in 1X PBS. Primary antibodies were diluted in 3% normal goat serum in 0.1% Triton and tissue was incubated on a shaker overnight at 4°C. Secondary antibodies were diluted in 3% normal goat serum and tissue was incubated on a shaker for 2 hours at room temperature. Brain sections were mounted on coverslips with ProLong Gold or Glass (Thermo Fisher) for all imaging. For staining with IFITM3 (Thermo Fisher #11714-1-AP), secondary antibody staining was done with goat anti-rabbit IgG, HRP-linked (Cell Signaling Technology #7074) and visualized with TSA Plus Cy3 detection system (Akoya Biosciences #NEL744001KT). For staining with SARS-CoV-2 Spike and N protein antibodies (GeneTex), an additional antigen retrieval step (70°C for 10min) was performed prior to blocking. Slides were imaged on an LSM 800 confocal microscope (Zeiss, Zen 2.6 software) using 20x, 40x, and 63x objectives. For analysis of phagocytic cups, slides were imaged on LSM 880 confocal microscope with AiryScan (Zeiss) using a 63x objective.

Fluorescent In Situ Hybridization (FISH): FISH experiments were performed using the RNAscope Multiplex Fluorescent Reagent Kit v1 assay for *Htra1* and v2 assay for *Grin1* and *Rbfox3* (ACD Bio) as described by the manufacturer for fixed-frozen tissue, but eliminating the 60°C incubation and post-fixation steps prior to tissue dehydration. Brains were embedded in OCT following 30% sucrose treatment and frozen at -80°C for a minimum of 1 day prior to sectioning. Mouse *Htra1* RNAscope Probe (ACD Bio #423711-C2), Mouse *Grin1* RNAscope Probe (ACD Bio #431611-C1) and mouse *Rbfox3* Probe (ACD Bio #313311-C2) were used to detect each transcript. For immunohistochemical labeling with antibodies following the RNAscope assay, tissues were incubated with blocking and antibody solutions as described above immediately after RNAscope and washing four times, 5 minutes each. Confocal optical sections were imaged on a Zeiss 700 at 63x magnification through layer IV of flattened *en face* cortical sections of the barrel cortex. The Htra1 channel was thresholded to remove puncta smaller than 0.06 um^2 in area, and the puncta within a 10 μm radius of each Aldh1l1-GFP+ astrocyte were counted. Three images each from at least two sections each of three separate mice were counted per condition.

Flow cytometry: For all flow cytometry experiments, animals were perfused transcardially with ice-cold D-PBS, mounted coronally in ice-cold isolation media (HBSS, 15 mM HEPES, 0.6% glucose, 1 mM EDTA pH 8.0) and 350 micrometer slices were prepared on a vibratome. A stereomicroscope was used to visually identify barrel regions; 1 mm^3 of tissue was collected per hemisphere. All data analysis was performed using FlowJo™ software.

For single cell sequencing of non-neuronal cells from the cortex, cells were isolated using a protocol modified from Adam et al 2017. Barrel cortex was enzymatically dissociated with psychrophilic proteases (PBS with 4 uL/mL DNAse (Sigma D4527-40KU), 5 mg/mL protease (Creative Enzymes NATE-0633, 175 ug/mL L-cysteine) incubated on ice for 20 minutes with gentle trituration every 5 minutes until tissue chunks were no longer visible. Cells were centrifuged at 300g for 5 minutes at 4°C.

For isolation of astrocytes and microglia with Papain, barrel cortex tissue was dissociated in 20 U/mL papain (Worthington) in dissociation buffer (Ca/Mg-free HBSS with phenol red, 1 mM L-cysteine, 22.5 mM D-glucose, 0.5 mM EDTA, 20 ug/mL DNAse) for 80 minutes at 34° C with shaking every 15 minutes. The dissociation reaction was stopped with 1 mg/ml ovomucoid trypsin inhibitor and the cells were pelleted by centrifugation at 300g for 5 minutes at room temperature. After removing the supernatant and triturating in fresh ovomucoid solution, myelin debris was eliminated by centrifuging in a 22% Percoll gradient at 900g for 20 minutes (acceleration 4, brake 1, 4° C). Pelleted cells were then washed with isolation medium and incubated in blocking solution consisting of anti-mouse CD16/32 antibody (Biolegend). Cells were sorted on a BD FACS Aria III and gated on forward/side scatter, live cells by Hoechst, CD11b-PE (eBioscience), and CD45-FITC (BioLegend) to identify, sort for, and enrich microglia. Microglia (CD11b+) and other cells were sorted into the blocking media described above and mixed at a ratio of 1/3 microglia: 2/3 non-microglial cells for 10x sequencing. Sorted cells were pelleted in an eppendorf tube at 300 g for 5 minutes at 4°C and then resuspended in blocking buffer consisting of 1% (weight/volume) RNase-free BSA and 1X PBS for downstream sequencing.

MACS Bead Isolation: For sorting microglia only for downstream RNA-sequencing, cells were isolated as described previously [135]. Briefly, barrel cortices dissected as described above were mechanically dissociated using a glass tissue homogenizer in isolation medium (HBSS, 15 mM HEPES, 0.6% glucose, 1 mM EDTA pH 8.0). Cells were filtered and then pelleted at 300 g for 10 minutes at 4°C before being resuspended in 22% Percoll (GE Healthcare) and centrifuged at 900 g for 20 minutes with acceleration set to 4 and deceleration set to 1 in order to remove cellular debris. Pelleted microglia were then resuspended in staining media (PBS, 0.5% BSA, 2 mM EDTA) and incubated with CD11b MACS beads (Miltenyi, 1:50) for 15 minutes at 4°C. The cells were washed with staining buffer, pelleted at 300 g for 5 minutes at 4°C, and reconstituted in 500 uL staining buffer. Microglia were isolated as described in the manual for MACS LS columns and collected in staining buffer without EDTA, pelleted at 300 g for 5 minutes at 4°C , counted on a hemocytometer, and 15,000-20,000 cells were diluted in 30 µL in a BSA-coated plate for 10x sequencing.

Single cell RNA-sequencing: Single cells were isolated as described above.

Pan-Glial isolation (Figure 1): Approximately 2,000 cells (v2, **Fig.**1-2) from each sample were loaded into each well of Chromium Chip A according to the manufacturer instructions and combined into droplets with barcoded beads using the Chromium controller. Libraries were prepared by the Gladstone Institutes Genomics Core following the instructions in the Chromium Single Cell 3’ Reagent Kits version 2 user guide. The samples were sequenced to an average depth of 40,000-60,000 reads on an Illumina HiSeq 4000 sequencer.

Microglial single cell sequencing (Figure 2): Approximately 15,000 cells were loaded into each well of Chromium Chip B (v3, figure 3), libraries were prepared in-house as described in the 10x Manual, and sequenced on one lane of the NovaSeq S4 at the Chan-Zuckerberg BioHub.

Single cell data analysis: Sequenced samples were processed using the Cell Ranger 2.1 pipeline (built on the STAR aligner)[136] and aligned to the GRCm38 (mm10) mouse reference genome. Clustering and differential expression analysis were conducted using Seurat version 3.1.4. Data for figures 1 and 2 (total glial population) and figure 3 (microglia only) were prepared on different versions of the 10x Chromium platform and were therefore analyzed separately as detailed below. Sequencing scripts can be found at https://github.com/lcdorman/IFNresponseCode, and original data can be found on GEO at GSE173173.

	Whole Glial Isolation	Microglial Isolation
Number of cells (thresholded)	1777 cells; 357 astrocytes	12,330 microglia
Figures	1, S2-S3	2-4, S4, S9
Age	Postnatal day 7	Postnatal days 5 and 7
Biological Replicates (mice)	1 Male + 1 Female	P5: 3 Male + 3 Female P7: 1 Male + 3 Female
Lanes	2 (Control/Deprived, 2 mice pooled)	4 (P5 Control/Deprived, 6 mice pooled; P7 Control/Deprived, 4 mice pooled)
10x Chromium Kit	Chip A/V2	Chip B/V3
Feature thresholds	400-5000 genes/cell	2500-7500 genes/cell
% Mitochondrial RNA thresholds	0-5% mitochondrial RNA/cell	0-7.5% mitochondrial RNA/cell
Normalization	SCTransform	Log normalization/scale factor 10,000
Minimum % of cells expressing gene for diff. exp. Analysis	5%	10%
Clustering resolution (Seurat)	1.2 (clusters); 0.1 (celltypes); 0.6 (astrocytes)	0.5

Sorted cells were sequenced using the 10x Chromium kit. Following alignment in Cell Ranger as described above, counts were imported into R and analyzed using the Seurat package [137,138]. Cells outside of the thresholds listed in the table were excluded from downstream analysis. Cells were identified as "female" or "male" based on their expression of the gene *Xist*; any cells expressing at leaste one count of *Xist* were labelled female, while all others were labelled male. Counts were then normalized, regressing out percent mitochondrial RNA and total counts per cell. The top 6000 most variable genes were used to calculate 50 principal components, and the top 30 PCs were used for nearest neighbor, UMAP, and cluster calculations with the resolutions shown in the table. Individual celltypes were identified through calculation of marker genes using the Wilcox test for genes expressed in at least 50% of cells in the cluster and a natural log fold change of 1.2 or greater and adjusted p value less than 0.001.

For the cold protease experiment examining all non-neuronal cells (Fig.1) , the astrocyte cluster was isolated and reclustered based on the top astrocyte and microglial genes to remove 5 cells which showed high expression of microglial marker genes and separate the cells into three clusters. The remaining astrocytes were re-normalized and analyzed with the Variance Partition package [139] in R to determine the top 1,000 genes altered by condition. Differential expression analysis using Seurat's MAST function was then conducted using these genes between the control-enriched and deprived-enriched clusters. Volcano plots were generated using the EnhancedVolcano package in R, with gene labels chosen from the top differentially expressed genes. Cutoffs were set at natural log fold change greater than 0.25 (28% increase) and adjusted p-value smaller than 10^{-3}.

For the microglia only experiment (Fig. 2-on) , the microglial and macrophage clusters were isolated based on expression of Cx3cr1, Fcrls, P2y12, and low expression of non-microglial genes as shown in the heatmap. The filtered cells were re-normalized and analyzed with the Variance Partition package ([139] in R to determine the top genes determining sex, the first 8 of which were excluded from downstream analysis. The top 6000 most variable genes were used to recalculate PCs, UMAP, and clusters. Clusters were determined using a resolution of 0.5, and the two sets of most closely related clusters (0/5 and 6/7) were combined due to low numbers of unique differentially expressed genes (log fold change >0.15, adjusted p-value < 10^{-5}). Clusters were combined either due to relatively low numbers of uniquely upregulated genes (<30 between clusters 6/7, 34 between clusters 0 and 5). The resultant and remaining clusters had equal or more unique DEGs and importantly were not more closely related to any other clusters with few unique DEGs. Differential gene expression between clusters were calculated using the MAST test in Seurat. The heatmaps shown only include genes expressed by at least 50% of the cells in that cluster and with an adjusted p-value below 10^{-25}, sorted by highest log fold change. GO analysis was conducted using the Metascape webpage (www.metascape.org) [140]. Volcano plots were generated using the EnhancedVolcano package in R, with gene labels chosen from the top differentially expressed genes. Cutoffs were set at natural log fold change greater than 0.2 (22% increase) and adjusted p-value smaller than 10^{-25}.

Cell cycle phase assignment: Cells were assigned to S phase, G1 phase, or G2/M phase (not distinguished) using a previously published dataset [134] and the CellCycleScoring function in Seurat.

"Eigengene" calculations: DAM/PAM Subset-specific "Eigengenes" were calculated based on published differential gene expression signatures. All genes differentially expressed in a particular published subset with LFC > 1.5 and adj. $p < 10^{-8}$ were combined and an expression value for this eigengene was calculated using the PercentageFeatureSet function in Seurat, which calculates a percent expression per cell for any gene set. Ribosomal genes, which are expressed by all the clusters, were excluded from the analysis to avoid biasing the eigengene towards these highly expressed genes. Eigengene expression was validated by randomly sampling sets of 10 genes from the eigengene; every random sample showed the same gene expression pattern in the clustered data set as the full gene set, ensuring that a few genes were not biasing the entire eigengene. The "Neuronal Eigengene" was calculated using a published cell-specific RNA sequencing database[122]. Fold enrichment by celltype (neurons, oligo lineage, astrocytes, microglia, endothelial cells) was calculated for each of the genes enriched in cluster 3 (MAST DE analysis, adj. p<1e-10, natural log fold change > 0.25). Fold enrichment by celltype was defined as the highest FPKM divided by the next highest FPKM for each gene, resulting in a cell type assignment and enrichment score. Only genes with an enrichment score greater than 3 for Neurons were included in the Neuronal eigengene calculation (45 genes). The normalized expression values for these 45 neuronal-specific genes were summed on a per-cell basis to create a violin plot showing overall neuronal gene expression per cluster.

RNA Velocity analysis: Spliced and unspliced transcript counts were calculated using Velocyto 0.17 and the velocyto run10x command with default settings. UMAP cell embeddings and annotation were exported from Seurat and used to plot all data shown. ScVelo 2.0.0 was run in Python and trajectories were calculated for all cells, then for each sample individually [69,141].

Bar plot creation: Bar plots were created using ggplot2 in R. Coding details are available on github (https://github.com/lcdorman/IFNresponseCode/blob/main/Code%20for%20paper/P5_P7%20Microglia/D_BarPlots.Rmd). A table was made of cells per cluster per sample. Cell numbers were normalized by sample by dividing each entry by the total number of cells for that sample and multiplying by 2,000. Percents per cluster were then calculated by dividing the normalized cell numbers by the total number of cells in that cluster and multiplying by 100. Statistics were calculated individually for each cluster using a Chi-Square test on the raw cell numbers per cluster and sample. Plots with multiple bars had an additional Bonferroni correction applied, which multiplies the p-value by the number of comparisons.

Atac-seq and microglial enrichment integration: “Microglial specificity” values were calculated using a published bulk sequencing dataset from developing mouse cortex[122]. FPKM values per gene in microglia were divided by the average FPKM for that gene in all other cell types to find a “Specificity score”. A specificity score of 10 or higher was considered “Microglial specific” for the purposes of this study. An unpublished Atac-seq study of bulk microglia from adult mouse cortex was used to identify open chromatin promoter peaks for each gene. Peaks were called using Homer. Homer’s “Peak Score” output was used to call peaks, which measures the position-adjusted number of reads identified for a particular promoter region. Only promoter peaks were considered, and if multiple promoter peaks were found for a single gene, only the one with the highest score was used. A promoter peak was only considered present if at least two of four samples had a peak score greater than 15. The minimum detectable peak had a value of 5, while the maximum detected was 5,000.

qPCR: To extract RNA from cells isolated by FACS, freshly sorted cells were pelleted at 500 g for 10 minutes at 4° and then resuspended in RLT Plus buffer (Qiagen). Cells were vortexed and frozen for at least one day at -80° before being thawed on ice and processed for RNA using an RNeasy Mini Kit (Qiagen). Purified mRNA was converted to cDNA with the High Capacity cDNA Reverse Transcription kit (Life Technologies) and amplified using either the Fast SYBR Green Master Mix (Thermo Fisher) or TaqMan Gene Expression Master Mix (Thermo Fisher) and a 7900HT Fast Real-Time PCR System (Applied Biosystems).

SARS-CoV-2 virus propagation and plaque assay: All SARS-CoV-2 cell culture and animals works were performed in the Biosafety level 3(BSL3). African green monkey kidney Vero-E6 cell line (ATCC#1586) and Calu-3 cells(ATCC# HTB-55) was obtained from American Type Culture Collection and maintained in Minimum Essential Medium (MEM, Gibco Invitrogen) supplemented with 10% fetal bovine serum (FBS, Gibco Invitrogen), 1% Penicillin-Streptomycin-Glutamine (Gibco Invitrogen) at 37 °C in a humidified 5% CO2 incubator. A clinical isolate of SARS-CoV-2 from a UCSF patient was propagated in Vero E6 cells and Calu-3 cells. 80% Confluent monolayers of Vero E6 cells grown in 6-well plates were incubated with the serial dilutions of virus samples (250 ul/well) at 37 °C for 1 hour. Next, the cells were overlayed with

1% agarose (Invitrogen) prepared with MEM supplemented containing 2% fetal bovine serum(sigma), 1x penicillin/streptomycin/glutamine (100xPSG, Gibco). Three days later, the cells were fixed with 4% formaldehyde (PFA) for 2 hours, the overlay was discarded and samples were stained with crystal violet dye.

SARS-CoV-2 infection: 5-6 weeks old Hemizygous K18-hACE2 mice (The Jackson laboratory, https://www.jax.org/strain/034860, stock number: 034860, B6.Cg-Tg(K18-ACE2)2Prlmn/J) were anesthetized with isofluorane and inoculated with 6x10^4 PFU of SARS-CoV-2 intranasally in a BSL3 facility. The mice were sacrificed at 3 and 6 days post- infection, and the brain was removed and fixed in 4% PFA for 72 hours before being sunk in 30% sucrose and embedded in OCT. 40 µm sections were cut on a cryostat and stained as described above with 2 minute antigen retrieval at 95 degrees. Antibodies used include the following: rabbit anti-SARS-CoV-2 Nucleocapsid(N) (GeneTex, GTX135361), mouse anti-SARS-CoV-2-spike(S), (GeneTex, GTX632604).

Microglia CD68 volume: Z-stacks were collected on an LSM 880 confocal microscope with AiryScan (Zeiss) on Superresolution mode and a 63x objective (NA 1.4). Laser power and gain were consistent across each image. AiryScan processing was performed in Zen software (Zeiss) at a setting of 6 (''optimal'' setting). Images were analyzed using Imaris software (Bitplane) by creating a 3D surface rendering of individual microglia, thresholded to ensure microglia processes were accurately reconstructed, and maintained consistent thereafter. Microglia rendering was used to mask and render the CD68 channel within each microglia. CD68 volume per microglia was then calculated as the total volume of masked CD68 volume within the masked GFP volume.

Microglia phagocytic compartment analyses: Phagocytic compartments, including phagocytic cups, phagosomes, and phagolysosomes, were identified as DAPI-enveloping structures that are distinct from the microglia nuclei. Unlike the microglia nuclear compartment, phagosomes lacked staining for Iba1 or GFP. Phagocytic cups lacked CD68 and only partially enveloped a DAPI+ and non-pyknotic cell. For experiments in 5xFAD animals, phagocytic cups were identified as Iba1 deficient organelles at the terminal ends of microglia processes. Microglia with bubble morphology were identified by enlarged and rounded phagosomes or phagolysosomes that were larger than the microglia nucleus. These phagocytic compartments contained DAPI+ nuclear material undergoing pyknosis or karyorrhexis, which were very sparsely distributed within the phagosome. In contrast, non-bubble phagosomes tightly enveloped engulfed nuclear material such that the DAPI signal saturated the phagosome area.

Z-stacks were acquired using an LSM 880 confocal microscope with AiryScan (Zeiss) on Superresolution mode and a 63x objective (NA 1.4, 0.04 µm pixel size, 16-bit depth) and processed as described above. Phagocytic compartments were analyzed in ImageJ and ROI's were drawn around phagosomes using the Versatile Wand Tool plugin. The "tolerance" setting was manually adjusted to envelop the microglia phagocytic compartment surface and "connectedness" was set to 8-connected. An optical section was selected from the z-stack that represented the center of the compartment and mean intensity, integrated density, and area were then recorded for each phagocytic compartment.

For analysis of phagocytic compartments in Sars-CoV-2 infected mice, images were first binned by average IFITM3 MFI per microglia. The maximum microglial IFITM3 mean fluorescence intensity per image across all samples was called 100%. The lower bin represents images with 0-50% of the maximum expression, and the higher bin represents images with 50-100% of the maximum expression. Each microglia was then manually scored for presence or absence of a phagocytic compartment as described above. For experiments in 5xFAD mice determining microglia association with plaques, microglia that were within 10 µm of an Aβ plaque was considered plaque-associated.

Lysotracker analysis: Mice were perfused with ice-cold PBS and cut into 200 µm coronal sections on a vibratome in a supplemented media (HBSS, 15 mM HEPES, 0.6% glucose, 1 mM EDTA pH 8.0). Sections containing the barrel cortex were incubated with Lysotracker Red at 1:5000 for 10 minutes, then washed and fixed overnight in 4% PFA before staining and mounting. 15 µm z-stacks were acquired on a LSM800 and analyzed in Fiji.

Interferon-β injection: A solution of 10 ng Interferon-β (IFN-β, R&D Systems, 8234-MB-010) diluted in 2 µl of aqueous solution containing 1mM of the indicator dye PsVue-550 (Molecular Targeting, P-1005, prepared according to the manufacturer's directions) was injected into the right lateral ventricle of P4 C57/Bl6J mice (coordinates: x = 1, y=1.8, z = -2, in reference to lambda). Control mice were injected with an equal volume PsVue-containing vehicle. The mice were perfused 24 hours later with ice-cold PBS and PFA, post-fixed in 4% paraformaldehyde overnight at 4°C, cryoprotected and sectioned on a cryostat at 50 µm (floating sections, used for IFITM3 quantification) and 20 µm (slide-mounted sections, used for 53BP1 foci quantification). Images were acquired using the 40x objective of an LSM 800 (Zeiss) and counted using the Cell Counter tool in Fiji. 53BP1 quantification was conducted on primary and secondary motor cortex Layer 2/3 within 500 µm laterally to the injection track.

Poly(I:C) microinjection into zebrafish larvae: For poly(I:C) injection, 7 dpf *Tg(mpeg:EGFP-CAAX);Tg(NBT:dsRed)* zebrafish larvae were anesthetized with 0.2 mg/ml of tricaine in embryo medium. Larvae were injected with 2 nl of 1 mg/ml poly(I:C) (Invitrogen) or PBS as a vehicle control into the optic tectal ventricle by microinjection. Zebrafish larvae were transferred to fresh embryo medium after injection for recovery and imaged at 4 hrs post injection. We carefully monitored the larvae after injection to confirm that they recovered from anesthesia and did not exhibit abnormal swimming behaviors. Only healthy post-injection larvae were used for live imaging.

Live imaging: For live imaging, *Tg(mpeg:EGFP-CAAX);Tg(NBT:dsRed)* zebrafish larvae were anesthetized with 0.2 mg/ml of tricaine in embryo medium and mounted in 1.2% low-melting agarose gel on a glass bottom 35-mm dish (MatTek) and covered with embryo water containing 0.2 mg/ml tricaine. Time-lapse image was performed on a Nikon CSU-W1 spinning disk/high speed widefield microscope. We took time-lapse images from the optic tectum collecting 40-60 µm z-stacks (step size: 0.5 µm) at 5 min intervals for 30 min-1 hr. The images were processed by ImageJ software. For analysis, we calculated the number of dsRed(+) neurons in microglia for the first 30 min of each video. For the analysis of process motility, we carefully observed each microglia process for the first 30 min of each video and classified all processes into three categories: 1) 'ramified' were defined as processes with or without movement that have no phagocytic cup formation, 2) 'cup formation' denoted processes with or without movement that contained or formed phagocytic cups, and 3) 'soma retraction' - processes that enclosed dsRed+

cells that were subsequently trafficked toward the microglial soma). Statistical analyses were performed by Graphpad Prism software.

- QUANTIFICATION AND STATISTICAL ANALYSIS

Graphpad Prism 9.3.1 was used for most statistical analyses of imaging data, and the Seurat package V3 in R was used for statistical analysis of single cell data. Statistical tests are as described in text and figure legends. Violin plots were used for data with n > 20 to better visualize the distribution of individual data points. Single cell RNA-sequencing data was analyzed in R as described in the methods section above. Categorical data shown in bar plots (cluster-specific differences in cell numbers) were analyzed in R using a Chi-Square test on each cluster with Bonferroni's correction for multiple comparisons.

RESOURCE TABLE

REAGENT or RESOURCE
Antibodies-immunostaining
rabbit anti-dsRed 1:1000 (Clontech, 632496)
Rat anti-mCherry 1:1000 (Invitrogen, M11217)
chicken anti-GFP 1:1000 (Aves Labs, 1020)
chicken anti-NeuN1:400 (Millipore, ABN91)
rabbit anti-Iba1 1:1000 (Wako Chemicals, 019-19741)
Mouse anti-Iba1 1:1000 (Wako Chemicals, 016-26721)
Guinea pig anti-Iba1 1:2000 (Synaptic Systems, 234-004)
Rat anti-P2ry12 1:100 (Biolegend, 848001)
rabbit anti-P2y12 1:500 (David Julius Lab)
rat anti-GFAP 1:1000 (Thermo Fisher, 13-0300)
Rabbit anti-IFITM3 1:1:1000 (Thermo Fisher, 11714-1-AP)
guinea pig anti-VGLUT2 1:2000 (Synaptic Systems, 135404)
rat anti-CD68 1:500 (BioRad, MCA1957GA)
Goat anti-rabbit IgG, HRP-linked (Cell Signaling Technology, 7074P2)
Hoechst 33342 solution 1:5000 (Thermo Fisher, 62249) was used for nuclear labeling
Mouse anti-Amyloid-Beta (4G8) 1:1000 (BioLegend, 800708)
rabbit anti-SARS-CoV-2-N protein 1:1000 (GeneTex, GTX135361)
mouse anti-SARS-CoV-2-Spike 1:1000 (GeneTex, GTX632604)
Rat anti-Bst2/Tetherin (R&D Systems, MAB8660-SP)
Mouse anti-γ-H2AX (EMD Millipore, 05-636)
Rabbit anti-53BP1 (Novus Biologicals, NB100-304)
Rabbit anti-cleaved caspase 3 1:1000 (BD Biosciences, 559565)
Goat Secondaries 1:500 (a-Rb, GP, Ck, Rat, Ms; 555, 488, 647) (Life Technologies)
Antibodies - flow cytometry
TruStain rat anti-CD16/32 1:100 (BioLegend, 101319)

APC rat anti-CD11b 1:100 (BioLegend, 101212)		
PE rat anti-CD11b 1:100 (eBioscience, 12-0112-81)		
FITC rat anti-CD45 1:100 (BioLegend, 103108)		
Rabbit anti-IFITM3 1:1:1000 (Thermo Fisher, 11714-1-AP)		
Goat anti-Rb 647 1:500 (Life Technologies A-21244)		
Critical Commercial Assays	Source	Cat #
RNAscope Multiplex Fluorescent Reagent Kit v1 assay, Mouse *Htra1* RNAscope Probe; RNAscope Multiplex Fluorescent Reagent Kit v2 assay, Mouse *Grin1* RNAscope probe, Mouse *Rbfox3* RNAscope probe	Advanced Cell Diagnostics	320851, 423711-C2, 323100 , 431611, 313311-C2
DeadEnd Fluorometric TUNEL system	Promega	G3250
Lysotracker Red	ThermoFisher	L7528
TSA Plus Cyanine 3, Cyanine 5, and Fluorescein detection kits	Akoya Biosciences	NEL744001KT, NEL745001KT NEL701A001KT
Chromium single cell gene expression platform, version 2 (Whole-glia RNAseq, Figure 1)	10x Genomics	Library and gel bead kit - V2, 120267 Chip A kit: 1000009
Chromium single cell gene expression platform, version 3 (Microglial RNAseq, Figures 2+)	10x Genomics	Library and gel bead kit – V3, 1000075 Chip B kit: 1000074
Summary of Deposited Data		
Single cell RNA-sequencing of glial from postnatal day 7 barrel cortex after unilateral whisker follicle cauterization at postnatal day 2	Gene Expression Omnibus	**GSE173173**
Single cell RNA-sequencing of microglia from postnatal day 5 and 7 barrel cortex after unilateral whisker follicle cauterization at postnatal day 2	Gene Expression Omnibus	**GSE173173**
Experimental Models: Model organisms		
Cx3cr1-GFP	JAX #00582	[142]
Aldh1l1-eGFP	GENSAT MGI:3843271	[143]
Ifnar1-/-	JAX #028288	[144]
Mx1-GFP	JAX #033219	[64]

Mx1-Cre	JAX #003556	[JAX]
Ai14	JAX #007908	[72]
B6.Cg-Tg(K18-ACE2)2Prlmn/J	JAX #034860	[102]
B6SJL-Tg(APPSwFlLon,PSEN1*M146L*L286V)6799Vas/Mmjax (5xFAD)	JAX #34840-Jax	[109]
Aldh1l1-tdTomato	MMRRC, RRID:MMRRC_036700-UCD	
Rorb-Ires2-Cre-D	Jax **023526**	
Tg(mpeg:EGFP-CAAX)	ZFIN ID: ZDB-TGCONSTRCT-191211-1	
Tg(NBT:dsRed)	ZFIN ID: ZDB-TGCONSTRCT-081023-2	